Title
Interactions of Virus Like Particles in Equilibrium and Non-equilibrium Systems

Author
Lin, Hsiang-Ku

Publication Date
2011

UNIVERSITY OF CALIFORNIA
RIVERSIDE

Interactions of Virus Like Particles in Equilibrium and Non-equilibrium Systems

A Dissertation submitted in partial satisfaction
of the requirements for the degree of

Doctor of Philosophy

in

Physics

by

Hsiang-Ku Lin

December 2011

Dissertation Committee:

    Dr. Roya Zandi , Chairperson
    Dr. Leonid Pryadko
    Dr. Umar Mohideen

The Dissertation of Hsiang-Ku Lin is approved:

_____

_____

_____
Committee Chairperson

University of California, Riverside

Acknowledgments

First and foremost I would like to thank my advisor, Roya Zandi, for fully supporting me from the past six years. Roya always teaches me how to think of a problem from the fundamental rules of physics when I was stuck with mathematical equations and formula. Not just being a mentor of physics, Roya also shares a lot of her own life experience with me and how to be strong in the real world!

I have been extremely lucky to have Dr. Lenoid Pryadko as my research advisor. He is the one who always provide hundred kinds of solutions when I have difficulties in my research. Dr. Pryadko tells things with very briefly but in a very smart way. After working with him for the past years, I indeed feel I improve myself into a higher level in physics. Thank you very much!

I would like to thank our colleague, Dr. Umar Mohideen, for performing the relevant experiment in his lab. From the discussion in our regular meetings between both experimental and theoretical groups, I can see how our theoretical work influences the experiments and the experiments in turn will help me to make my theory more realistic. I'm grateful to make myself being part of the joint theoretical-experimental work.

I also would like to thank to Dong Gui, who has patiently and insistently performing biological experiments. I can see how hard he has been trying to solve endless problems to make our project work out. A-Gui, all the efforts will eventually be paid off! I am very positive!

My best luck in Riverside is to have all my dear friends. It would never have been easy to study in United States without all your support. Too many friends' names are shown in my brain. I'll never forget our great friendship and keep in touch with you all!

Last, I must thank my family, who are the ones love me most in the world. Because of their understanding and support, I can do what I love most in United States. I'll never have

achieve any success without them.

Peng, you always are the most matters and important to me!

To my parents for all the support.

ABSTRACT OF THE DISSERTATION

Interactions of Virus Like Particles in Equilibrium and Non-equilibrium Systems

by

Hsiang-Ku Lin

Doctor of Philosophy, Graduate Program in Physics
University of California, Riverside, December 2011
Dr. Roya Zandi , Chairperson

This thesis summarizes my Ph.D. research on the interactions of virus like particles in equilibrium and non-equilibrium biological systems.

In the equilibrium system, we studied the fluctuation-induced forces between inclusions in a fluid membrane. We developed an exact method to calculate thermal Casimir forces between inclusions of arbitrary shapes and separation, embedded in a fluid membrane whose fluctuations are governed by the combined action of surface tension, bending modulus, and Gaussian rigidity. Each objects shape and mechanical properties enter only through a characteristic matrix, a static analog of the scattering matrix. We calculate the Casimir interaction between two elastic disks embedded in a membrane. In particular, we find that at short separations the interaction is strong and independent of surface tension.

In the non-equilibrium system, we studied the transport and deposition dynamics of colloids in saturated porous media under un-favorable filtering conditions. As an alternative to traditional convection-diffusion or more detailed numerical models, we consider a mean-field description in which the attachment and detachment processes are characterized by an entire spectrum of rate constants, ranging from shallow traps which mostly account for hydrodynamic dispersivity, all the way to the permanent traps associated with physical straining. The model has

an analytical solution which allows analysis of its properties including the long time asymptotic behavior and the profile of the deposition curves. Furthermore, the model gives rise to a filtering front whose structure, stability and propagation velocity are examined. Based on these results, we propose an experimental protocol to determine the parameters of the model.

Contents

List of Figures

Chapter 1

Introduction

As the most fundamental type of biological entities, viruses or macromolecules such as proteins, exist almost in every ecosystem on earth. They constantly change the properties of the dwelling biological system by interacting with the surrounding medium. The studies of the mechanisms of their interactions are crucial for us to elucidate how biological systems work and provide better ideas to solve many actual problems caused by them, for example illnesses.

Viruses or macromolecules always carry complex structures and demonstrate diverse properties, which usually can not be generalized within simple rules. However, from another point of view, as actual physical identities, they must be governed by fundamental physics laws. When we consider the interactions between the virus or macromolecules or the interactions between them and the surrounding medium, there are generalized mechanisms of the interactions that can be applied to the biological entities of any kind. Therefore, in our studies, we modeled real virus or macromolecules into microscopic particles, which possess the most simplified structure resembling to the real entities. In this thesis, I will demonstrate our studies on the interactions of the microscopic biological particles in two major systems, which are equilibrium and non-equilibrium systems.

In the equilibrium system, we study the thermal fluctuation-induced force between two foreign inclusions in a biological fluid membrane. Every living cell is enclosed by a membrane. Typical biological membranes consist of amphiphilic molecules as a lipid bilayer. Many kinds of macromolecules such as proteins are often found embedded in the membrane structure, which are essential for a cells survival. For instance, some specific proteins embedded in the membrane allow the cell to communicate with others while some proteins work as tiny motors directing the flow of substance, like nutrients, in and out of the cell. Several studies also reveal that many cell diseases might be associated with the malfunction of protein-membrane interactions.

As a fluid object, the cell membrane is subject to random fluctuations, which modulate the interactions between embedded proteins. The study of fluctuation-induced forces between proteins in a fluid membrane could greatly be simplified by the use of continuum elasticity theory, which enables us to accurately describe the membrane as a complex object. In general, a biological membrane can be modeled as a two-dimensional sheet of fluid surface, which closely resembles the surface of a sea. The elastic waves, here, are due to the thermal fluctuations of the membrane. In the absence of embedded proteins, a membrane can freely fluctuate without any constraints. However, the presence of proteins will modify the spectrum of the allowed fluctuations resulting in a set of novel interactions. Understanding these novel forces by utilizing analytical methods to describe the complexities of biological membranes and its constituents is the goal of this work.

In the non-equilibrium system, we study the transport and deposition dynamics of the virus like particles (VLPs) in saturated porous media under unfavorable filtering conditions. Many processes in biological systems involve the transport and filtration of particles through media. The fundamental mechanism behind the kinetics of these filtration processes is the interactions between the VLPS and the media, which are represented by a variety of forces

2

exerted on VLPS. Due to the complexity of the dwelling environment of VLPS in the non-equilibrium system, it is almost impossible to describe the kinetics of these filtration processes by directly solving the equations of motion of the VLPS due to all these interactions.

The phenomenological mean-field models based on the convection-diffusion equation (CDE), however, provides a possible method in the study of these non-equilibrium processes. Typically, the CDE method models the dynamics of free particles in terms of the average drift velocity v and the hydrodynamic dispersivity λ, while the net particle deposition rate r_d accounting for particle attachment and detachment at trapping sites is a few-parameter function of local densities of free and trapped particles. Nevertheless, the CDE model has significant problems that can not explain some of the experimental phenomena [50, 51, 52].

Our mean-field model of such system considers a description in which the attachment and detachment processes are characterized by an entire spectrum of rate constants, ranging from shallow traps which mostly account for hydrodynamic dispersivity, all the way to the permanent traps associated with physical straining. This provides an alternative to traditional convection-diffusion or more detailed numerical models. Our model has an analytical solution which allows analysis of its properties including the long-time asymptotic behavior and the profile of the deposition curves. Furthermore, the model gives rise to a filtering front whose structure, stability, and propagation velocity are examined. These analytical solutions provide us better results in fitting with the experimental data.

Chapter 2

Fluctuation-induced forces between inclusions in a fluid membrane under tension

2.1 introduction

A biological membranes are quasi-two-dimensional structures formed by amphiphilic lipid molecules with embedded macromolecules such as proteins [1]. Studies indicates that many biological functions strongly depend on the geometry, topology, and dynamics of the structures of biological membranes. Specialized proteins exert the necessary control in cellular tasks such as exocytosis, cell adhesion, etc [2]. The behavior of proteins in a fluid membrane is determined by interactions between them[3, 4, 5, 6, 7, 8, 9, 13]. For the past years, both experimental and simulation results have been observed that the aggregations of membrane proteins [10, 11, 12]. However, the physical mechanism of the phenomena is still not well understood yet. The possible candidates for the interaction forces can be divided into two classes:

the direct forces comprising the electrostatic forces and Van der Waals forces, and the indirect forces (curvature-mediated forces) including elastic forces and fluctuation-induced forces[4, 5]. While the elastic force is caused by membrane equilibrium shape deformation, the fluctuation-induced force is due to embedded proteins whose presence suppresses the thermal fluctuations. The fluctuation-induced force, which we will somewhat loosely call the Casimir force, is the focus of this work.

Thermal Casimir forces have been a topic of intense research and development efforts over the past two decades[4, 5, 6, 7, 8], However, protein-protein interaction and membrane-protein interaction resulting from membrane thermal fluctuations are still not fully understood. Most importantly, previous theoretical research considered the fluctuations in the presence associated with the membrane rigidities exclusively. Although surface tension is negligible for free-floating membranes in equilibrium with lipid molecules in the solution[4, 5], the interactions stemming from surface tension could dominate bending force under certain conditions. For example, the surface tension is finite for a cell membrane with excess osmotic pressure or, for the experiment where membrane is stretched by a hydrophobic frame and the concentration of the free lipids in solvent is very low. The area of the membrane must change when it fluctuates. Thus, it is necessary to consider the cost of the surface tension energy[14, 15]. In Ref. [14], it is shown that the surface tension can span as much as five orders of magnitudes depending on the external forces applied to the membrane. It is interesting to note that even though the Casimir interactions due to surface tension were considered previously by Kardar group [6], the interactions resulting from bending rigidities were ignored in the work. From a theoretical point of view, understanding the fluctuation-induced forces in membranes due to the bending forces combined with the surface tension is a very challenging task. Furthermore, the previous studies were focused only on two regimes in which the bending rigidities of embedded inclusions are either infinity (stiff inclusions) or close to those of the surrounding membrane[4, 5, 7, 8].

In this work, we present a method of calculating the fluctuation-induced forces between any number of elastic inclusions for a fluid membrane governed by both surface tension and bending energy. This method is based on the technique for Casimir forces in antiferromagnets[16]. The Green's function technique is applied to calculate the force in conjunction with scattering-matrix approach[17]. We find that the Casimir interaction energy can be regarded as the responses of the thermal fluctuation fields to the sources at inclusions' edges. The sources are expressed in terms of multipoles which contains the information of inclusions' shapes and boundary conditions.

As a given example, we calculate the Casimir energy between two elastic disks in membrane. We examine the unexplored parameter range where both surface tension and bending energy are relevant. In the limit of very small separations, it is necessary to keep the multipoles with large angular momentums. We reproduce the same distance dependency as that obtained through Derjaguin or proximity force approximation (PFA) [18]. At large separations, the Casimir energy is mainly contributed by lower order of multipoles. We also derive explicit asymptotics for the Casimir interaction. Results are checked against the previous theoretical work in the weak- and strong- coupling regimes for the cases dominated by surface tension or bending energy[4, 5, 8, 7]. Full results are given in Fig 2.1. For non-zero surface tension energy, we find that the Casimir energy is strongly suppressed at large distance. Furthermore, as seen in the figure, at large separations the Casimir effect is significantly determined by the characteristic length defined as square root of the ratio between the bending rigidity (κ_0) and surface tension (σ_0) of the membrane[9, 19],

$$\ell_0 \equiv \alpha_0^{-1} = (\kappa_0/\sigma_0)^{1/2}. \tag{2.1}$$

while at small separations it is dominated by the ratio of bending rigidities between the inclusion and the ratio regardless of the characteristic length.

The chapter is organized as follows. In Sec. 2.2, we derive a general formula for the thermal Casimir energy between inclusions of arbitrary shapes and separations. The Green's function technique is introduced with the help of Hellmann-formula to calculate the thermal Casimir energy. This formula can be further recast in a similar form to that of scattering matrix approach employed to calculate quantum Casimir energy[20]. In Sec. 2.3, we calculate the Casimir interaction between two elastic disks embedded in a membrane. The full numerical results at whole regimes and the analytical results are at large separations in surface tension or bending energy dominated regimes are presented in Sec. 2.4. At last, we give summary in Sec. 2.5.

2.2 Method

2.2.1 Hamiltonian for small deformation membrane with inclusions

We consider a fluid membrane with any number of inclusions of arbitrary shapes and separations undergoing thermal fluctuations. The membrane surface can be described as a height function $u(x, y)$ or $u(\vec{r})$, the out-of-plane displacement above the reference plane x-y plane, $z = 0$. With the small deformation of a fluid membrane, the energy is expanded to the quadratic order in the displacement with the equilibrium membrane configuration assumed to be flat. Inclusions are modeled as thin isotropic elastic solid characterized by in-plane Lamé coefficients and bending rigidities. The fluid membrane does not transmit in-plane stress perturbations. Thus, the in-plane displacements of the inclusions do not interact, and only the transverse displacements $z \equiv u(x, y)$ are relevant for Casimir interaction. We find that the corresponding part of the energy for the membrane with the inclusions has the standard Helfrich

form [21, 22],

$$U \equiv \int_{\mathcal{A}} d^2\mathbf{r} \, \frac{\sigma}{2}(\nabla u)^2 + \frac{\kappa}{2}(\nabla^2 u)^2 + \bar{\kappa}[u''_{xx}u''_{yy} - (u''_{xy})^2] + \oint_{\mathcal{S}} dl \, \frac{\gamma}{2r^2}(u'_\theta)^2 \qquad (2.2)$$

where primes (') denote the partial derivatives with respect to x or y as indicated. The integration is performed over the projected area $\mathcal{A}$ of the entire membrane. $\sigma \equiv \sigma(\vec{r})$ stands for surface tension, $\gamma \equiv \gamma(\vec{r})$ denotes line tension, and $\kappa \equiv \kappa(\vec{r})$ and $\bar{\kappa} \equiv \bar{\kappa}(\vec{r})$ represent the bending and Gaussian rigidities respectively. Thermodynamical stability require that $\sigma, \kappa > 0$ and $-2\kappa \leq \bar{\kappa} \leq 0$.

The first term in Eq. (2.2) has the standard form of a surface-tension contribution. However, inside inclusions, it refers to the elastic energy associated with the in-plane stress induced by membrane surface tension. Energy cost of elastic deformations of the inclusion is due to stretching (or compressing) and shearing effects. To ensure local stability of the system, line tension energy at boundaries has to be added in Hamiltonian. From Appendix A.1, we derive effective surface tension of a circular inclusion embedded in a fluid membrane. The terms with κ and $\bar{\kappa}$ represent the bending energy contributions associated with the mean and the Gaussian curvatures respectively. Typical values of the bending rigidity κ is around $0.1 - 25k_BT$[23].

2.2.2 Green's function technique

Next, we introudce our Green's function technique to calculate the Casimir-like forces between inclusions in a fluid membrane. The membrane sheet creates its own fluctuation spectrum due to the thermal energy. Using the standard variational method, we find a symmetric

8

(real Hermitian) differential operator $\hat{\mathcal{H}} \equiv \hat{\mathcal{H}}_r$, where

$$\hat{\mathcal{H}}_r = \kappa(\mathbf{r})\nabla^4 - \sigma(\mathbf{r})\nabla^2$$

as a functional derivative of the energy Eq. (2.2) with respect to $u(\mathbf{r})$. The corresponding set of orthonormal eigenfunctions $u_n \equiv u(\mathbf{r})$, $\hat{\mathcal{H}}u_n = E_n u_n$ is complete in membrane system,

$$\sum_n u_n(\mathbf{r})u_n(\mathbf{r}') = \delta(\mathbf{r} - \mathbf{r}')$$

We define the Green's function (GF) of the operator $\hat{\mathcal{H}}$,

$$\hat{G} \equiv G(\mathbf{r}, \mathbf{r}') = \sum_n \frac{u_n(\mathbf{r})u_n(\mathbf{r}')}{E_n} \tag{2.3}$$

which obeys the usual equation

$$\mathcal{H}_r G(\mathbf{r}, \mathbf{r}') = \delta(\mathbf{r} - \mathbf{r}').$$

Any fluctuation states can be expressed in terms of eigenfunctions,

$$u(\mathbf{r}) = \sum A_n u_n(\mathbf{r}) \tag{2.4}$$

where A_n is fluctuation amplitude of flu. Substituting Eq. (2.4) into Eq. (2.2), we obtain the total energy in terms of eigenenergy,

$$U = \sum_n A_n^2 E_n$$

9

Then the partition function can be written as a standard Boltzmann sum over all the membrane state configuration,

$$\mathcal{Z} = \int \mathcal{D}A_n \exp[-\sum_n \beta A_n^2 E_n] \tag{2.5}$$

where $\beta = 1/k_B T$. We obtain the following expression for the free energy increment associated with the inclusions,

$$\mathcal{F} = -\frac{1}{2\beta} \sum_n \ln \beta E_n + \text{Constant} \tag{2.6}$$

To apply our Green's function technique to calculate the Casimir free energy, we model the inclusions as regions where the parameters of Eq. (2.2) different from those in the surrounding part of the membrane, e.g. $\kappa \equiv \kappa_0 + \lambda \kappa_1$, etc., where position-independent σ_0, κ_0, and $\bar{\kappa}_0$ correspond to an unperturbed membrane and $\sigma_1(\mathbf{r})$, $\kappa_1(\mathbf{r})$, and $\bar{\kappa}_1(\mathbf{r})$ vanish outside of the inclusions. The line tension at boundaries is defined as $\gamma = \lambda \gamma_1(\mathbf{r})|_{\mathbf{r}\in\mathcal{S}}$. The coefficient λ parametrizes the amplitude of the perturbation. Thus, the Hamiltonian can be divided into two parts,

$$\hat{\mathcal{H}} \equiv \hat{\mathcal{H}}_\lambda = \hat{\mathcal{H}}_0 + \lambda \hat{\mathcal{V}}(\sigma_1, \kappa_1, \bar{\kappa}_1) \tag{2.7}$$

where the first term $\hat{\mathcal{H}}_0$ describes the total energy of free membrane and the second term $\lambda \hat{\mathcal{V}}$ represents the potential due to the presence of foreign inclusions. The non-perturbed fluid membrane corresponds to $\lambda = 0$. The free energy difference depends on parameter λ and can be calculated as an integral of its derivative with respect to λ by using

$$\Delta \mathcal{F}_\lambda \equiv \mathcal{F}_\lambda - \mathcal{F}_0 = \int_0^\lambda d\lambda' \frac{\partial \mathcal{F}}{\partial \lambda'} = \frac{1}{2\beta} \sum_n \int_0^{\lambda'} d\lambda' \frac{\frac{\partial E_n}{\partial \lambda'}}{E_n} \tag{2.8}$$

where $\partial_\lambda E_n / E_n$ is obtained by taking derivative of Eq. (2.6) with respect to λ. Using the

Hellmann-Feynman theorem[24, 25], the derivative term in Eq. (2.8) gives

$$\frac{\partial E_n^\lambda}{\partial \lambda} = \langle u_n^\lambda | \frac{\hat{\mathcal{H}}}{\partial \lambda} | u_n^\lambda \rangle = \langle u_n^\lambda | \hat{\mathcal{V}} | u_n^\lambda \rangle \tag{2.9}$$

we obtain the following expression for the free energy

$$\beta \Delta \mathcal{F}_\lambda = \frac{1}{2} \int_0^\lambda d\lambda' \mathrm{Tr}(\hat{\mathcal{V}} \hat{G}_{\lambda'}) \tag{2.10}$$

Explicitly, with the energy functional (2.2), we have

$$
\begin{aligned}
\mathrm{Tr}(\hat{\mathcal{V}} \hat{G}) &= \int d^2 \mathbf{r} \left\{ \sigma_1(\mathbf{r})[\nabla \cdot \nabla' \hat{G}] + \kappa_1(\mathbf{r}) \nabla^2 (\nabla')^2 \hat{G} \right. \\
&+ \left. \overline{\kappa}_1(\mathbf{r}) \left[\partial_x^2 \partial_{y'}^2 \hat{G} + \partial_{x'}^2 \partial_y^2 \hat{G} - 2\partial_x \partial_y \partial_{x'} \partial_{y'} \hat{G} \right] \right\}_{\mathbf{r}'=\mathbf{r}} + \oint_{\mathcal{S}} dl \left\{ \frac{\gamma}{r^2} \partial_\theta \partial_\theta' \hat{G} \right\}_{\theta=\theta'},
\end{aligned}
$$

It is evident that the exact expression (2.10) performs an integration only over the area occupied by the inclusions. In the case of k membrane inclusions, we write $\hat{\mathcal{V}} = \sum_{l=1}^k \hat{\mathcal{V}}_l$, where the operator $\hat{\mathcal{V}}_l$, $l = 1, 2, \cdots, k$, is only non-zero inside the inclusions. The full Green's function in Eq. (2.10) can be expanded into the series in powers of λ,

$$\hat{G}_\lambda \equiv \hat{G}_0 - \lambda \hat{G}_0 \hat{\mathcal{V}} \hat{G}_0 + \lambda^2 \hat{G}_0 \hat{\mathcal{V}} \hat{G}_0 \hat{\mathcal{V}} \hat{G}_0 - \cdots. \tag{2.11}$$

Substituting Eq. (2.11) into Eq. (2.10) we obtain

$$\beta \Delta \mathcal{F} = -\frac{1}{2} \sum_{n>0} \frac{(-\lambda)^n}{n} \mathrm{Tr}[(\hat{\mathcal{V}} \hat{G}_0)^n] \tag{2.12}$$

where $1/n$ results from the integration. The term with $(-\lambda)^n$ in Eq. (2.12) inside the trace can

be expressed as

$$\hat{\mathcal{V}}_{l_1}\hat{G}_0\hat{\mathcal{V}}_{l_2}\hat{G}_0\cdots\hat{\mathcal{V}}_{l_i-1}\hat{G}_0\hat{\mathcal{V}}_{l_i}\hat{G}_0\cdots\hat{\mathcal{V}}_{l_n}\hat{G}_0 \tag{2.13}$$

where $1 \le l_i \le k$. Here we should emphasize that each operator $\hat{\mathcal{V}}_{l_i}$ in Eq. (2.13) acts on GFs to the left and to the right of it, with subsequent integration over the area of the inclusions. Every time if the index of the operator $\hat{\mathcal{V}}_{l_i}$ acting the GFs is different from that of its neighbor $\hat{\mathcal{V}}_{l_{i+1}}$, i.e. $l_i \ne l_{i+1}$, it introduces the factor of $1/R$ to the Casimir energy (R is the distance between two inclusions). Let us denote the exact GF in the presence of only one inclusion.

$$G_\lambda^{(l)} \equiv G_0 - \lambda G_0\hat{\mathcal{V}}_l G_0 + \lambda^2 G_0\hat{\mathcal{V}}_l G_0\hat{\mathcal{V}}_l G_0 - \cdots. \tag{2.14}$$

Thus the relevant Casimir free energy for k inclusions becomes

$$\beta\Delta\mathcal{F}_\lambda = -\frac{1}{2}\sum_{\{l_1\}}\text{Tr}[\log(1+\lambda\hat{\mathcal{V}}_{l_1}\hat{G}_\lambda^{(l_1)})] + \sum_{s>1}\frac{(-\lambda)^s}{2s}\sum_{\{l_i\}}\text{Tr}\,\hat{\mathcal{V}}_{l_1}G_\lambda^{(l_1)}\hat{\mathcal{V}}_{l_2}G_\lambda^{(l_2)}\ldots\hat{\mathcal{V}}_{l_s}G_\lambda^{(l_s)}, \tag{2.15}$$

where the n-th term involves the summation over s inclusion indices $1 \le l_i \le k$, with the neighboring indices different, $l_{i+1} \ne l_i$, $l_s \ne l_1$. Comparing term-by-term the corresponding expansion in powers of λ, it is easy to check that Eq. (2.15) is equivalent to Eq. (2.12). Derivation details are provided in Appendix A.3. To evaluate the series in Eq. (2.15), we introduce the "hopping" matrix

$$\Sigma_{ll'} \equiv (1-\delta_{ll'})\hat{\mathcal{V}}_l G_\lambda^{(l)} \tag{2.16}$$

Rewrite the sum in the nth term as

$$\text{Tr}\,\hat{\Sigma}^n \equiv \sum_{\{l_i\}}\text{Tr}\,\Sigma_{l_1 l_2}\Sigma_{l_2 l_3}\ldots\Sigma_{l_{n-1}l_n}\Sigma_{l_n l_1}, \quad n>1, \tag{2.17}$$

where neighboring indices are different. The free energy can then be written as

$$\Delta \mathcal{F}_\lambda = \sum_l \Delta \mathcal{F}_\lambda^{(l)} + \mathcal{F}_\mathrm{C}, \tag{2.18}$$

where

$$\beta \mathcal{F}_\mathrm{C} \equiv \frac{1}{2} \operatorname{Tr} \log\left(\mathbb{I} + \lambda \hat{\Sigma}\right). \tag{2.19}$$

The first term indicates the self-energies of individual inclusions while the second term describes the Casimir free energy between inclusions. The full expression of $\hat{\Sigma}$ matrix can be written as following,

$$\hat{\Sigma} = \begin{pmatrix} 0 & \Sigma_{12} & \cdots & \cdots & \Sigma_{1s} \\ \Sigma_{21} & 0 & \cdots & \cdots & \Sigma_{2s} \\ \cdots & \cdots & \cdots & \cdots & \cdots \\ \cdots & \cdots & \cdots & \cdots & \cdots \\ \Sigma_{s1} & \cdots & \cdots & \cdots & 0 \end{pmatrix}$$

Note that the diagonal elements of the matrix $\hat{\Sigma}$ are vanished. Each element Σ_{ij} indicates the interaction between ith and jth inclusions, which is decomposed in terms of multipole expansions. Although Σ_{ij} is in principle complicated, it is still computed for certain geometries. We will give an example in the following section.

Quite remarkably, Eq. (2.19) provides the most general result to calculate the Casimir energy between a finite number of compact objects of arbitrary shape and separation. The idea of physics involved can be obtained from a discussion of the response of an object to the thermal fluctuation fields, which records the information about the material properties and boundary conditions and is related to the scattering fields by the object. We decomposed the energy as multipole-multipole interaction energy, which only enters though the matrix Σ_{ij}. This result can

also be recast in a form similar to that of the scattering matrix approach employed to calculate the electromagnetic Casimir interaction[17].

2.3   Example: Casimir energy for two disks embedded in membrane

As an example, we, here, focus on the interaction between two circular disks embedded in a membrane. The geometry is shown in Fig. A.2. In this case, the $\hat{\Sigma}$ matrix in Eq. (2.19) is a 2×2 matrix since there are only two inclusions,

$$
\hat{\Sigma} = \begin{pmatrix} 0 & \lambda\Sigma_{12} \\ \lambda\Sigma_{21} & 0 \end{pmatrix} = \begin{pmatrix} 0 & \lambda\hat{\mathcal{V}}_1\hat{G}_\lambda^{(1)} \\ \lambda\hat{\mathcal{V}}_2\hat{G}_\lambda^{(2)} & 0 \end{pmatrix}
$$

Then Eq. (2.19) becomes

$$
\begin{aligned}
\beta\mathcal{F}_{\mathrm{C}} &= \frac{1}{2}\,\mathrm{Tr}\,\log(\mathbb{I} - \lambda^2\hat{\mathcal{V}}_1 G_\lambda^{(1)}\hat{\mathcal{V}}_2 G_\lambda^{(2)}) \\
&= -\frac{1}{2}\sum_s \frac{\mathrm{Tr}[\lambda^2\hat{\mathcal{V}}_1 G_\lambda^{(1)}\hat{\mathcal{V}}_2 G_\lambda^{(2)}]^s}{s},
\end{aligned} \tag{2.20}
$$

which can be interpreted as a series of back-and-forth interactions between inclusions. To evaluate Eq. (2.20), we first construct the the exact GF in the presence of a single circular inclusion as a series in polar coordinates. For a free membrane, the corresponding energy operator is $\hat{\mathcal{H}}_0 = \kappa_0(\nabla^4 - \alpha_0^2\nabla^2)$, with $\alpha_0^2 \equiv \sigma_0/\kappa_0$. The uniform-membrane GF is a combination of GFs for the Laplace and Helmholtz equations[19],

$$
G_0(r) = -\frac{1}{2\pi\sigma_0}\big[K_0(\alpha_0 r) + \ln(\alpha_0 r)\big], \quad r \equiv |\mathbf{r} - \mathbf{r}'|. \tag{2.21}
$$

14

A simple use of the multipole expansion of Eq. (2.21), we expand the modified Bessel function and logarithm in a power series,

$$\ln |\mathbf{r} - \mathbf{r}'| = \ln R_> - \sum_{m>0} \frac{R_<^m}{R_>^m} \frac{\cos m\phi}{m},$$

and

$$K_0(\alpha|\mathbf{r} - \mathbf{r}'|) = K_0(\alpha R_>)I_0(\alpha R_<) + 2\sum_{m>0} K_m(\alpha R_>)I_m(\alpha R_<)\cos m\phi.$$

Here we denote $R_< \equiv \min(r, r')$, $R_> \equiv \max(r, r')$, $\phi \equiv \phi - \phi'$ is the angle between the two vectors. Thus, the general solution for the GF with a single disk associated with the angular harmonic $\cos m\phi$ or $\sin m\phi$ contain four radial functions, $r^{\pm m}$ and the modified Bessel functions $K_m(\alpha r)$ and $I_m(\alpha r)$, which gives

$$
\begin{aligned}
2\pi\sigma_0 G_\lambda^{\text{in}}(\mathbf{r}, \mathbf{r}') &= \sum_{m\geq 0} \left[C_m(r')r^m + D_m(r')I_m(\alpha r) \right] \cos(m\phi), \\
2\pi\sigma_0 G_\lambda^{\text{out}}(\mathbf{r}, \mathbf{r}') &= A_0 - \ln R_> + B_0 K_0(\alpha_0 r) - K_0(\alpha_0 R_>)I_0(\alpha_0 R_<) \\
&\quad + \sum_{m>0} \left\{ A_m \frac{1}{r^m} + \frac{1}{m}\frac{R_<^m}{R_>^m} + B_m K_m(\alpha_0 r) - 2K_m(\alpha_0 R_>)I_m(\alpha_0 r_<) \right\} \cos m\phi.
\end{aligned}
$$

Here we assume that $r' > a$ and denote $R_< \equiv \min(r, r')$, $R_> \equiv \max(r, r')$, ϕ is the angle between the two vectors. It also requires four boundary conditions on the circumference: continuity of the function, normal derivative, as well as the following two quantities,

$$\sigma\partial_r u - \kappa\partial_r \left(\nabla^2 u\right) + \frac{\bar{\kappa}}{r}\partial_r \left(\frac{1}{r}u''_{\theta\theta}\right) - \frac{\gamma}{r^2}\partial u''_{\theta\theta}\bigg|_{in} = u - \kappa\partial_r \left(\nabla^2 u\right) + \frac{\bar{\kappa}}{r}\partial_r \left(\frac{1}{r}u''_{\theta\theta}\right)\bigg|_{out},$$

(2.22)

15

and

$$\kappa \nabla^2 u + \frac{\bar{\kappa}}{r}\left(\frac{1}{r}u''_{\theta\theta} + \partial_r u\right)\bigg|_{in} = \kappa \nabla^2 u + \frac{\bar{\kappa}}{r}\left(\frac{1}{r}u''_{\theta\theta} + \partial_r u\right)\bigg|_{out}. \tag{2.23}$$

Here $u''_{\theta\theta}$ is the second derivative over the polar angle with respect to the center of the disk. The detailed derivation of the boundary conditions of Eqs. (2.22) and (2.23) is shown in Appendix A.4. After applying the boundary conditions, the relevant Green's function can be expressed in the form as

$$2\pi\sigma_0 G_\lambda^{\text{in}}(\mathbf{r},\mathbf{r}') = \sum_{m\mu,\alpha\beta} c_{m\mu}^{(\alpha\beta)} f_{m\mu}^{(\alpha)}(\mathbf{r}) g_{m\mu}^{(\beta)}(\mathbf{r}'), \tag{2.24}$$

where

$$f_{m\mu}^{(1)}(\mathbf{r}) = r^m(\cos m\theta, \sin m\theta)_\mu,$$

$$f_{m\mu}^{(2)}(\mathbf{r}) = I_m(\alpha r)(\cos m\theta, \sin m\theta)_\mu,$$

$$g_{m\mu}^{(1)}(\mathbf{r}') = (r')^{-m}(\cos m\theta', \sin m\theta')_\mu,$$

$$g_{m\mu}^{(2)}(\mathbf{r}') = K_m(\alpha_0 r')(\cos m\theta', \sin m\theta')_\mu.$$

From Eq.(2.20), for $s = 1$ let us rewrite

$$\text{Tr}[\lambda^2 \hat{\mathcal{V}}_1 G_\lambda^{(1)} \hat{\mathcal{V}}_2 G_\lambda^{(2)}] = \text{Tr}[\lambda^2 \hat{\mathcal{V}}_1 \sum_m u_m(\mathbf{r})u_m(\mathbf{r}') \hat{\mathcal{V}}_1 \sum_q v_q(\boldsymbol{\rho})v_q(\boldsymbol{\rho}')] \tag{2.25}$$

$$= \text{Tr}[\sum_{m,q} (\lambda v_q(\boldsymbol{\rho}')\hat{\mathcal{V}}_1 u_m(\mathbf{r}))(\lambda u_m(\mathbf{r}')\hat{\mathcal{V}}_2 v_q(\boldsymbol{\rho}))] \tag{2.26}$$

where we simply rewrite $G_\lambda^{(1)} \equiv \sum_m u_m(\mathbf{r})u_m(\mathbf{r}'), G_\lambda^{(2)} \equiv \sum_m v_m(\boldsymbol{\rho})v_m(\boldsymbol{\rho}')$. Since trace is invariant under cyclic permutations, Eq. (2.25) can be written in the form as Eq. (2.26). To do so, the interaction energy is obtained because the operator $\hat{\mathcal{V}}^{(i)}$ is acting on both Green's functions, $\hat{G}_\lambda^{(1)}$ and $\hat{G}_\lambda^{(2)}$. Then, the term with $s = 1$ in Eq. (2.20) can be evaluated by replacing

16

$\lambda^2 \hat{\mathcal{V}}_1 G_\lambda^{(1)} \hat{\mathcal{V}}_2 G_\lambda^{(2)}$ with Eq. (2.26) and then further simplified after several integrations by parts (see Appendix A.5 and Appendix A.6), which gives

$$\beta \mathcal{F}_C = -\frac{1}{2} \sum_\nu \sum_{s=1}^{\infty} \frac{\text{Tr}[\hat{\Lambda}^\nu \hat{\Lambda}^\nu]^s}{s} = \frac{1}{2} \ln \prod_\nu \det(1 - \hat{\Lambda}^\nu \hat{\Lambda}^\nu) \qquad (2.27)$$

each element in the $\hat{\Lambda}^\nu$ is found to be

$$\hat{\Lambda}_{nm}^\nu = \begin{pmatrix} -A_n^f \frac{m \binom{m+n-1}{m}}{R^q} & A_n^g \frac{K_{m+n}(\alpha_0 R) + (-1)^\nu K_{m-n}(\alpha_0 R)}{2} \\ -B_n^f \frac{m \binom{m+n-1}{m}}{R^q} & B_n^g \frac{K_{m+n}(\alpha_0 R) + (-1)^\nu K_{m-n}(\alpha_0 R)}{2} \end{pmatrix} \qquad (2.28)$$

where the coefficients $A_n^f, A_n^g, B_n^f, B_n^g$ are defined in Eq. (A.22) and can be obtained applying boundary conditions. The full expressions are listed in Appendix A.7. The symbol ν indicates the sum over odd and even solutions. The element $\hat{\Lambda}_{nm}^\nu$ is denoted by a 2×2 matrix owing to the combined solutions of the GFs of the Laplace and Helmholtz equations.

For the numerics, we keep a finite number of azimuthal angular harmonics, m. The Casimir energy at large separation is mainly contributed by low order of multipoles and can be computed in a few terms of Eq. (2.27) on the requirement of accuracy. As the separation become smaller, higher order multipole interaction become more relevant. The manipulation of large matrices $\hat{\Lambda}$ is needed.

2.4   Results

2.4.1   Analytical results and discussions

In the absence of line tension at the inclusion boundaries, the diagonal components of the equilibrium stress tensor in the inclusions coincide with the surface tension of the membrane, which gives $\sigma = \sigma_0$ in Eq. (2.2). For a non-zero surface tension, we find that the Casimir energy

becomes strongly suppressed at distances R larger than the characteristic length ℓ_0, Eq. (2.1).

Note that the Casimir energy retains the power-law asymptotic form

$$\beta\,\mathcal{F}_{\mathrm{C}} = -A\,a^n/R^n, \quad \beta \equiv 1/k_B T, \quad R \gg a, \tag{2.29}$$

with the exponent increasing from $n = 4$ at $R \lesssim l_0$ (bending-energy-dominated regime) to $n = 8$ at $R \gtrsim l_0$ (tension-dominated regime). This is illustrated in Fig. 2.1 for two inclusion stiffnesses, with a number of different surface tensions. Depending on the parameters, the Casimir free energy scaled with the fourth power of the distance has either constant or $\propto 1/R^4$ asymptotics.

Analytical results for Casimir energy (2.27) can be obtained in weak coupling regime (κ/κ_0, $\bar{\kappa}/\bar{\kappa}_0 << 1$) regardless of any separation or any coupling regime but large separation compared to the inclusion size a. The corresponding Casimir energy can be further simplify the calculations by replacing $G_\lambda^{(l)}$ with the bare GF G_0, which gives

$$\begin{aligned} \beta\,\mathcal{F}_{\mathrm{C}} &= \frac{1}{2}\,\mathrm{Tr}\,\log(\mathbb{I} - \lambda^2\hat{\mathcal{V}}_1 G_0 \hat{\mathcal{V}}_2 G_0) \\ &= -\frac{1}{2}\sum_n \frac{\lambda^{2n}}{n}\,\mathrm{Tr}[\hat{\mathcal{V}}_1 G_0 \hat{\mathcal{V}}_2 G_0]^n, \end{aligned} \tag{2.30}$$

The obtained full analytical expressions are too cumbersome to quote here. We only present simplified results for three important parameter ranges, and illustrate the general trends in Fig 2.1 where we plot the distance dependence of the Casimir energy in the scaling relation Eq. (2.29) with $n = 4$. Note that the results at small separations are checked against those obtained through PFA which we will discuss the details in the next section.

(a) $l_0 >> R$, regime dominated by the bending energy. At large separation, the

18

Casimir energy Eq. (2.27) has the asymptotic form (2.29) with $n = 4$ and the coefficient

$$A = (4B_2^g + A_0^f)B_2^g, \qquad (2.31)$$

$$B_2^g = \frac{\overline{\kappa}_0 - \overline{\kappa}}{4\kappa_0 + \overline{\kappa}_0 - \overline{\kappa}}, \quad A_0^f = \frac{4(\kappa - \kappa_0) + 2(\overline{\kappa} - \overline{\kappa}_0)}{2\kappa + \overline{\kappa} - \overline{\kappa}_0}.$$

Discontinuity in $\overline{\kappa}$ is required for the leading order result. The general expression (2.31) reproduces the same results obtained in previous work. In the strong coupling limit, where κ and $-\overline{\kappa}$ are infnite (stiff inclusion), we find the $A = 6[4, 5, 8, 7]$; in the weak coupling, it gives $A = -\lambda^2 \kappa_1 \overline{\kappa}_1 / 2\kappa_0^2 [4, 5, 8]$.

(b) $\ell_0 \ll a \ll R$, regime dominated by the surface tension of the membrane. We find that the leading-order power law term in a/R (resulting from dipole-like fluctuations around the inclusions) is zero, and the next-order terms give the Casimir energy (2.30) falling off much faster, $\mathcal{F}_C \propto 1/R^8$, with the coefficient proportional to $\overline{\kappa}_1^2$. The full result being too bulky, we only present the strong-coupling limit,

$$\beta \Delta \mathcal{F}_C = -9(a/R)^8$$

which is in agreement with Refs. [26, 27], and the leading-order contribution in λ at weak-coupling,

$$\beta \mathcal{F}_C^{(2)} = -\frac{36\lambda^2 \overline{\kappa}_1^2 a^4}{\sigma_0^2 R^8} = -\frac{36(\overline{\kappa} - \overline{\kappa}_0)^2 a^4}{\sigma_0^2 R^8}. \qquad (2.32)$$

Note that we also obtain the same power law in the presence of line tension energy, in which case Eq. (2.2) has $\sigma \neq \sigma_0$ inside inclusions. See Fig. 2.2. In a special case where the tilt motion of the inclusion is restricted, we recover the Casimir energy $\beta \Delta \mathcal{F}_C = -a^4/R^4$ at large separation (See Fig. 2.1).

(c) $a \lesssim \ell_0 \lesssim R$, with both surface tension and bending rigidities of the membrane

19

relevant. The full analytical Casimir energy contains terms decaying like a power of separation R, and exponential decaying term as $K_m(R/l_0)$. In particular, for $l_0 << R$, the modified Bessel function become exponentially small. In this case the Casimir energy is proportional to $1/R^8$. The exponentially small terms become relevant when $\ell_0 \sim R$, where Casimir energy crosses over to the small-σ regime (**a**) with $\mathcal{F}_C \propto 1/R^4$. This crossover can be seen in Fig. 2.1. A representative case corresponds to $\ell_0 = 10a$, where $A \equiv -(R/a)^4 \mathcal{F}_C$ is nearly constant for $R \lesssim \ell_0$, is strongly reduced for larger R, and eventually crosses over to $\propto 1/R^4$ ($\mathcal{F}_C \propto 1/R^8$) for $R \gg \ell_0$. At smaller R, the same asymptotic power law is also seen, e.g., for $\ell_0/a = 1$.

Note that the distance dependence of the Casimir energy is the same, $\propto 1/R^8$, as long as $\ell_0 \ll R$, which includes regimes (**b**) and (**c**). In the regime (**b**), dominated by the surface tension, this power law can be easily obtained by treating the inclusions as point-like objects in the effective field theory (EFT)[27]. For inclusions that are free to tilt with the membrane, the expansion starts with the quadrupole terms[27]. In the regime (**c**) the higher-order multipole terms in the EFT expansion diverge as increasing powers of $\ell_0/a \gg 1$. However, the contributions to the Casimir energy coming from higher-order multipole terms also get suppressed as increasing powers of $1/R$. As a result, the leading-order quadrupole terms dominate, which again gives $\mathcal{F}_C \propto 1/R^8$ for $\ell_0 \ll R$. For $\ell_0 \sim R$, where we recover the exponentially small terms $\propto K_m(R/\ell_0)$, all multipoles contribute equally and the EFT approach cannot be used.

2.4.2 Casimir energy at small separation: our method and PFA

For the R dependence of the Casimir energy at short separation, as shown in the Fig. , the Casimir energy becomes large in this regime. Note that the R dependence of the Casimir energy does not depend on the characteristic length ℓ_0 but determined by the ratio κ/κ_0. As seen in Fig 2.1, all the symbol and solid lines representing the fixed values of the ratio κ/κ_0 converge together respectively when the separation become very small. The small

separation asymptotic form of the Casimir energy can also be evaluated within Derjaguin[18]

or proximity force approximation (PFA) where the Casimir energy is calculated between curved

contact lines in terms of the interaction between parallel and infinitesimal straight line segments

(see Fig. A.3). We calculate the analytical results of the Casimir energy per unit length for two

half-planes with the separation H based on the previous work in Ref. [20] and we obtain

$$\frac{\mathcal{F}}{k_B T l} = \frac{f}{H} + \mathcal{O}(H) \tag{2.33}$$

where $f = \pi/24$ in the limit dominated by the surface tension energy and $f \approx 0.46$ in the

limit dominated by the bending energy. f for the intermediate regime can also be calculated by

numerical integration of Eq. (A.23). However, with the Hamiltonian of Eq. (2.2) the bending

energy dominated limit is relevant at very short separation. Thus, for two hard disks, PFA gives

$$\beta \mathcal{F}_{\mathrm{PFA}} = -\pi f \left[x^{-1/2} + \frac{1}{2} - \frac{3}{8} x^{1/2} + \mathcal{O}(x) \right], \quad x \equiv \frac{H}{a}. \tag{2.34}$$

The details of the evaluations are provided in Appendix A.8. To compare the results between

our method and PFA, we plot the ratio of the Casimir energy, $\mathcal{F}_C$[Eq. (2.27)] calculated for

different cutoff m (highest order of multipole) in the regime dominated by bending energy,

and $\mathcal{F}_{PFA}$[Eq. (2.34)] in Fig. (2.3). It can be seen that the ratio $\mathcal{F}_C/\mathcal{F}_{PFA}$ approaches one

only at very short separation. Clearly, the PFA approximation is only valid in the limit of small

distances. The figure also shows that higher order multipoles are necessary at shorter separations

as expected.

2.5 Summary

In conclusion, we have developed an exact method for computing the Casimir energy between elastic inclusions of arbitrary shapes embedded in a biological membrane under tension, characterized by the surface tension σ_0 and bending and Gaussian rigidities, κ_0 and $\overline{\kappa}_0$. The method allows to calculate the Casimir forces in all ranges of parameters and for all separations. The Casimir energies are fully characterized by the objects' "scattering" matrices, which encode the shapes and mechanical properties. In particular, for two elastic disks, the Casimir energy scales as $\propto 1/R^4$ for $R \lesssim \ell_0$, and crosses over to $\propto 1/R^8$ for $R \gtrsim \ell_0$. At short distances, the Casimir energy is large; for hard disks our findings agree with the corresponding PFA results, $\mathcal{F}_C \propto H^{-1/2}$. One interesting result is that the Casimir energy is strongly suppressed for inclusions whose Gaussian rigidity $\overline{\kappa}$ equals that of the membrane.
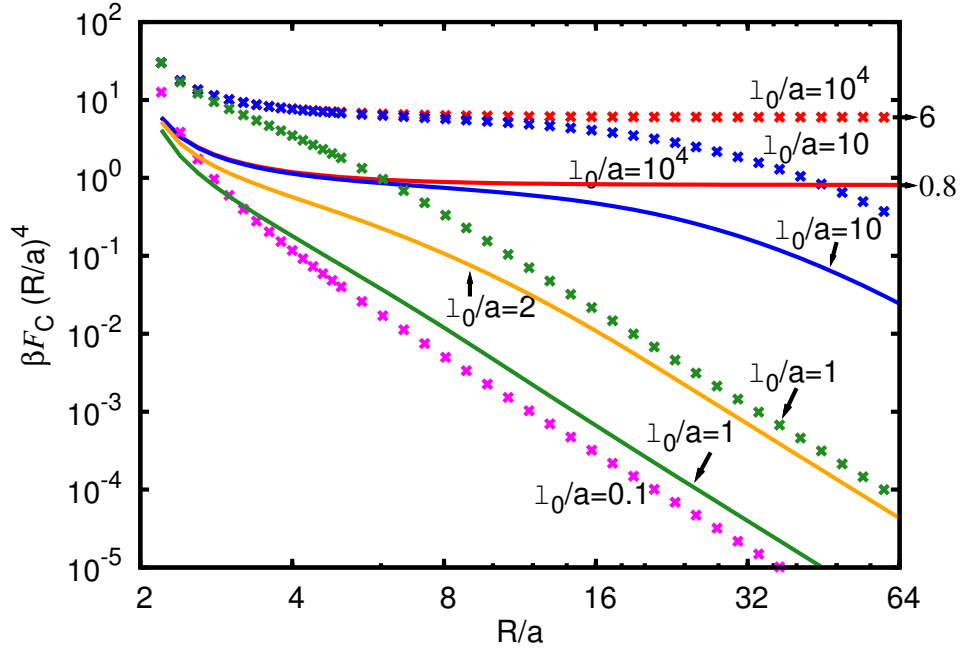
Figure 2.1: (color online) The Casimir free-energy (2.30) scaled with fourth power of the distance as a function of R/a for $\kappa/\kappa_0 = 10^4$ (symbols) and $\kappa/\kappa_0 = 10^{-1}$ (solid lines), with $\alpha_0 a \equiv a/\ell_0$ as indicated. We set $\overline{\kappa}_0 = -\kappa_0$, $\overline{\kappa} = -\kappa$. Dashed black lines indicate asymptotic large-R dependences evaluated with Eq. (2.31). Plots are horizontal ($\Delta\mathcal{F} \propto R^{-4}$) only for $R \lesssim \ell_0 \equiv \alpha_0^{-1}$; for larger R/ℓ_0 the Casimir energy decays as $\Delta\mathcal{F} \propto R^{-8}$.
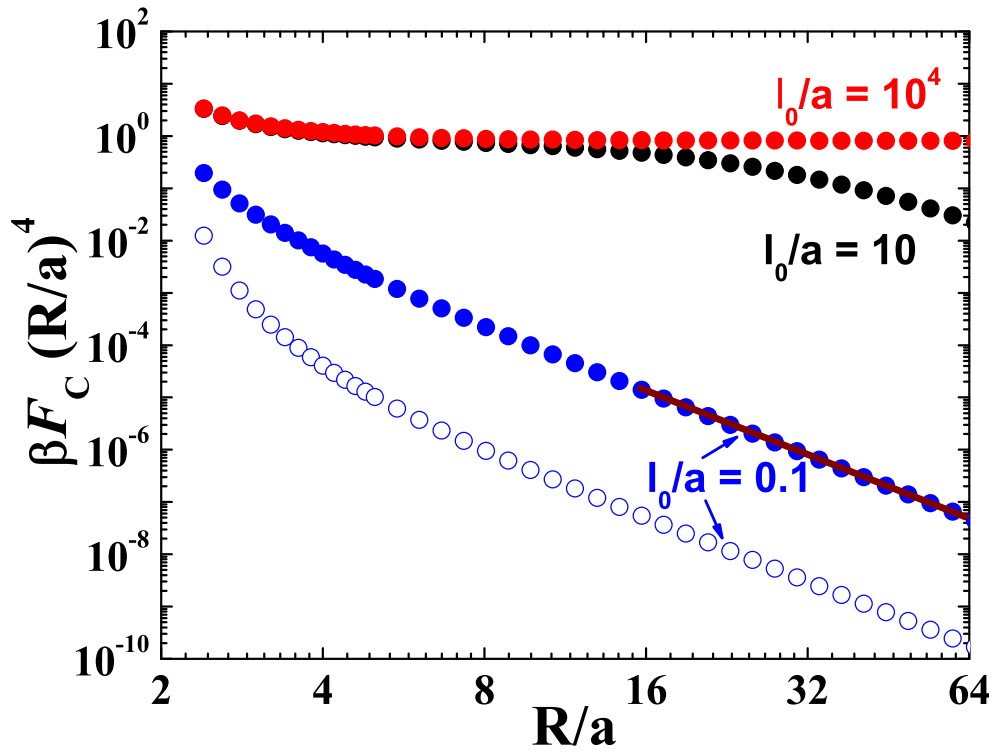
Figure 2.2: (color online) The Casimir free-energy (2.30) scaled with fourth power of the distance as a function of R/a for $\kappa/\kappa_0 = 10^{-1}$, with $\alpha_0 a \equiv a/\ell_0$ as indicated. We set $\overline{\kappa}_0 = -\kappa_0$, $\overline{\kappa} = -\kappa$. Empty symbol line indicates the Casimir energy with $\sigma_0 = \sigma$ while solid symbol lines indicate that with different surface tensions. The solid brown line shows that the Casimir energy decays as $\Delta\mathcal{F} \propto R^{-8}$ in surface tenison dominated regime.
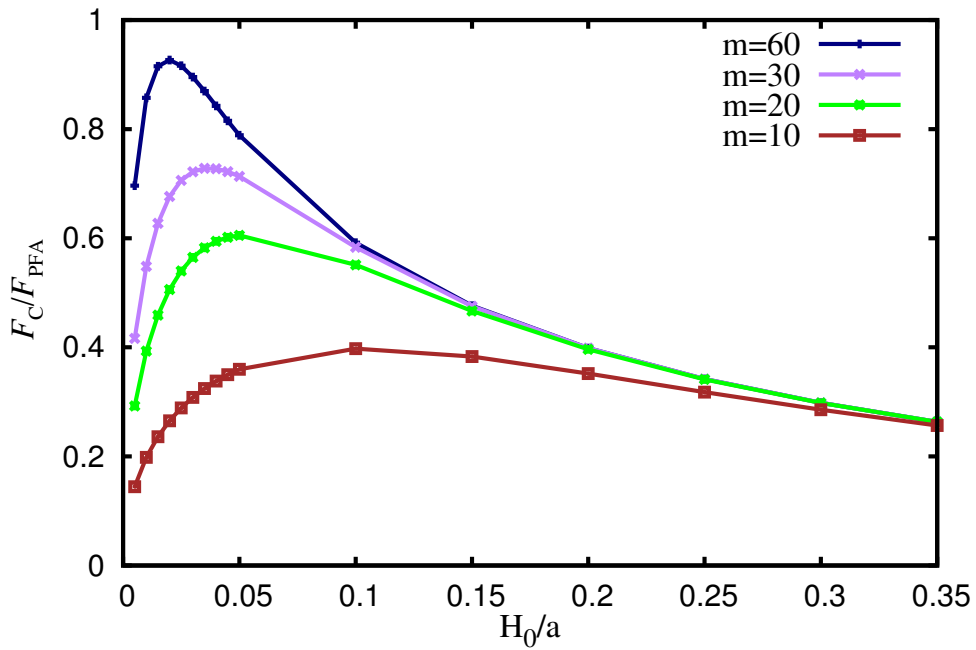
Figure 2.3: The Casimir energy of two disks in the regime dominated by the bending energy ($\ell_0/a = 10^4$, $\kappa/\kappa_0 = 10^4$) divided by the PFA estimate (2.34). The quantity m indicates the multipole order of truncation. Clearly, the PFA approximation is only valid in the limit of small distances. The figure shows that higher order multipoles are necessary at shorter separations as expected.

Chapter 3

Attachment and detachment rate distributions in deep-bed filtration

3.1 Introduction

Many processes in biological systems as well as in the chemical and petroleum industry involve the transport and filtration of particles in porous media with which they interact through various forces[28, 29, 30, 31]. These interactions often result in particle adsorption and/or entrapment by the medium. Examples include filtration in the respiratory system, groundwater transport, in situ bioremediation, passage of white blood cells in brain blood vessels in the presence of jam-1 proteins, passage of viral particles in granular media, separation of species in chromatography, and gel permeation. The particle-medium interactions in these systems are not always optimal for particle retention. For example, the passage of groundwater through soil often happens under chemically unfavorable conditions, and as a result many captured particles (e.g., viruses and bacteria) may be released back to the solution. While filtration under favorable conditions has been studied and modeled extensively[32, 33, 34, 35, 36, 37, 38, 39, 40, 41], we

are just beginning to understand the process occurring under unfavorable conditions.

Several models have been developed to describe the kinetics of particle filtration under unfavorable conditions. The most commonly used ones are, in essence, phenomenological mean-field models based on the convection-diffusion equation (CDE) [see Eq. (3.1) and Sec. 3.2]. Typically, one models the dynamics of free particles in terms of the average drift velocity v and the hydrodynamic dispersivity λ, while the net particle deposition rate r_d accounting for particle attachment and detachment at trapping sites is a few-parameter function of local densities of free and trapped particles. For given filtering conditions, the parameters λ and v can be determined from a separate experiment with a tracer, while the coefficients of the function r_d can be obtained by fitting Eq. (3.1) to the breakthrough curves.

Despite their attractive simplicity, it is widely accepted now that the phenomenological models at the mean-field level have significant problems. First, the depth dependent deposition curves for viruses and bacteria are often much steeper than it would be expected if the deposition rates were uniform throughout the substrate[42, 43, 44, 45, 46, 47, 48, 49]. This was commonly compensated by introducing the depth-dependent deposition rates. The problem was brought to light in Ref. [50], where it was demonstrated that the steeper-than-expected deposition rates under unfavorable filtering conditions also exist for inert colloids.

Second, Bradford et al. [51, 52] pointed out that the usual mean-field models based on the CDE, accounting for dynamic dispersivity and attachment and detachment phenomena, cannot explain the shape of both the breakthrough curves and the subsequent filter flushing. In these experiments some particles were retained in the medium, and the authors argued for the need to include the straining (permanent capture of colloids) in the model. Even so, these models may still be insufficient to fit the experiments [53].

More elaborate models to describe deep-bed filtration have been proposed in Refs. [54, 55, 56, 57]. These models go beyond the mean-field description by simulating subsequent filter

27

layers as a collection of multiply connected pipes with a wide distribution of radii, which results in a variation in flow speed and also of the attachment and detachment rates (even straining in some cases). The disadvantage of these models is that they are essentially computer based: it is difficult to gain an understanding of the qualitative properties of the solutions, without extensive simulations. Furthermore, the simulation results suffer from statistical uncertainties.

In the present work, we develop a minimalist mean-field model to investigate filtering under unfavorable conditions. The model accounts for both a convective flow and the primary attachment and detachment processes. Unlike the previous mean-field models of filtration, our model contains attachment sites (traps) with different detachment rates B_i [see Eq. (3.32)], which allows an accurate modeling of the filtration dynamics over long-time periods for a broad range of inlet concentrations. Yet, the model admits exact analytical solutions for the profiles of the deposition and breakthrough curves which permit us to understand qualitatively the effect of the corresponding parameters and design a protocol for extracting them from experiment.

One of the advantages of our model is that the "shallow" short-lived traps represent the same effect as hydrodynamical dispersivity without generating unphysically fast moving particles or requiring an additional boundary condition at the inlet of the filter. The "deep" long-lived traps allow to correctly simulate long-time asymptotics of the released colloids in the effluent during a washout stage. The traps with intermediate detachment rates determine the most prominent features of breakthrough curves. The effect of every trap kind is to decrease the apparent drift velocity. As attachment and detachment rate constants depend on colloid size, we can also account for the apparent acceleration of larger particles without any microscopic description as in Ref. [58]. The particle-size distribution can be also used to analyze the steeper deposition profiles near the inlet of the filter [43, 44, 49, 50].

The paper is organized as follows. In Sec. 3.2, we give a brief overview of colloid-transport experiments, CDE models, and their analytical solutions in simple cases. The lin-

earized multirate convection-only filtration model is introduced in Sec. 3.3. The model is characterized by a discrete or continuous trap-release-rate distribution; it is generally solved in quadratures, and completely in several special cases. The results support our argument that the hydrodynamic dispersivity can be traded for shallow traps. This serves as a basis for the exact solution of the full mean-field model for filtration under unfavorable conditions introduced in Sec. 3.4, where we show that a large class of such models can be mapped exactly back to the linearized ones and analyze their solutions, as well as the propagation velocity, structure, and stability of the filtering front. We suggest an experimental protocol to fit the parameters of the model in Sec. 3.5 and give our conclusions in Sec. 3.6.

3.2 Background

3.2.1 Overview of colloid transport experiments

A typical setup of a colloid-transport experiment is shown in Fig. 3.1. A cylindrical column packed with sand or other filtering material is saturated with water running from top to bottom until the single-phase state (no trapped air bubbles) is achieved. At the end of this stage, colloidal particles are added to the incoming stream of water with both the concentration of the suspended particles and the flow rate kept constant over time T. This is sometimes followed by a filter washout stage in which clean water is pumped through the filter. The filtration processes are characterized by two relevant experimental quantities: the particle breakthrough and deposition profile curves. While breakthrough curve represents the concentration of effluent particles at the outlet of the column as a function of time, deposition curves illustrate the depth distribution of concentration of the particles retained throughout the column.
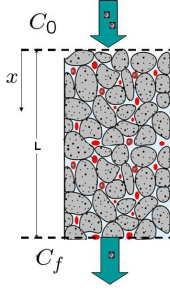
29

Figure 3.1: Schematic of experimental setup in the colloid-transport studies.

3.2.2 Convection-diffusion transport model

As the suspended particles move through the filtering column, each individual colloid follows its own trajectory. Consequently, even for small particles that are never trapped in the filter, the passage time through the column fluctuates. In the case of laminar flows with small Reynolds numbers and sufficiently small particles, which presumably follow the local velocity lines, the passage time scales inversely with the average flow velocity along the column v. The effects of the variation between the trajectories of particles as well as their speeds can be approximated by the velocity-dependent diffusion coefficient $D = \lambda v$, where λ is the *hydrodynamic dispersivity* of the filtering medium. In comparison, the actual diffusion rate of colloids in experiments is negligibly small. Dispersivity is often obtained through tracer experiments in which the motion of the particles, i.e., salt ions, which move passively through the filter medium without being trapped, is traced as a function of time.

Overall, the dynamics of the suspended particles along the filter can be approximated by the mean-field CDE,

$$\frac{\partial C}{\partial t} + v\frac{\partial C}{\partial x} - \lambda v\frac{\partial^2 C}{\partial x^2} = -r_d, \tag{3.1}$$

where $C \equiv C(x,t)$ is the number of suspended particles per unit water volume averaged over the filter cross section at a given distance x from the inlet and r_d is the deposition rate which may include both attachment and detachment processes.

30

3.2.3 Issues with the CDE approximation

The diffusion approximation employed in Eq. (3.1) has two drawbacks which could seriously affect the resulting calculations if enough care is not used.

First, while the diffusion approximation works well to describe the concentration $C(x, t)$ of suspended particles in places where $C(x, t)$ is large, it seems to significantly overestimate the number of particles far downstream where $C(x, t)$ is expected to be small or zero. This is mainly due to the fact that the diffusion process allows for infinitely fast transport, albeit for a vanishingly small fraction of particles. In the simple case of tracer dynamics [$r_d = 0$ in Eq. (3.1)], the general solutions as presented in Eqs. (3.6) and (3.7) are non-zero even at very large distances $x - vt \gg 2(\lambda vt)^{1/2}$. While in many instances this may not be crucial, the application of the model to, e.g., public health and water safety issues might trigger a false alert.

Second, for the filtering problem one expects the concentration $C(x, t)$ to be continuous, with the concentration downstream uniquely determined by that of the upstream. On the other hand, Eq. (3.1) contains second spatial derivative, which requires in addition to the knowledge of $C(x, t)$ at the inlet, $x = 0$, another type of boundary condition to describe the concentration of particles along the column. This additional boundary condition could be, e.g., the spatial derivative $C'(x, t)$ at the inlet, $x = 0$, or the outlet, $x = L$ [59, 49], or the fixed value of the concentration at the outlet. We show below that fixing a derivative introduces an incontrollable error. On the other hand, we cannot introduce a boundary condition for the function $C(x, t)$ at the outlet, $x = L$, as this is precisely the quantity of interest to calculate.

The situation has an analogy in neutron physics[60]. While neutrons propagate diffusively within a medium, they move ballistically in vacuum. A correct calculation of the neutron flux requires a detailed simulation of the momentum distribution function within a few meanfree paths from the surface separating vacuum and the medium. In contrast to the filtration

theory, for the case of neutron scattering, where the neutron distribution is stationary it is common to use an approximate boundary condition in terms of a "linear extrapolation distance" (the inverse logarithmic derivative of neutron density).

The CDE [see Eq. (3.1)] can be solved on a semi-infinite interval ($x_{\max} \gg L$) with setting $C'(x,t) = 0$ at $x_{\max}$ and calculating the value of $C(x,t)$ at $x = L$ as an approximation for the concentration of effluent particles. To illustrate this situation, we solve Eq. (3.1) for the case of tracer particles, where the deposition rate is set to zero, $r_d = 0$. We consider a semi-infinite geometry with the initial condition $C(x,0) = 0$ and a given concentration $C(0,t)$ at the inlet. The corresponding solution is presented in Sec. 3.2.4. The spatial derivative at the boundary given in Eq. (3.9) is non-zero, time-dependent, and rather large at early stages of evolution when the diffusive current near the boundary is large. Therefore, setting an additional boundary condition for the derivative, e.g., $C'(0,t) = 0$, is unphysical.

On the other hand, the problem with the boundary condition far downstream, $C(x_{\max}, t) = 0$, $x_{\max} \gg L$, can be ill-defined numerically, as this condition is automatically satisfied to a good accuracy as long as the bulk of the colloids has not reached the end of the interval.

3.2.4 Tracer model

The simplest version of the convection-diffusion equation [Eq. (3.1)] applies to tracer particles where the deposition rate is set to zero, $r_d = 0$,

$$\frac{\partial C}{\partial t} + v\frac{\partial C}{\partial x} - \lambda v \frac{\partial^2 C}{\partial x^2} = 0. \tag{3.2}$$

With the initial conditions, $C(x,0) = 0$, the Laplace-transformed function $\tilde{C} \equiv \tilde{C}(x,p)$ obeys the equation

$$p\tilde{C} + v\tilde{C}' - \lambda v \tilde{C}'' = 0, \tag{3.3}$$

where primes denote the spatial derivatives, $\tilde{C}' \equiv \partial_x \tilde{C}(x, p)$. The solution to the above equation is $\tilde{C} \propto e^{\kappa x}$, with

$$\kappa_\pm = \frac{1}{2\lambda} \pm \left(\frac{1}{4\lambda^2} + \frac{p}{\lambda v} \right)^{1/2}. \tag{3.4}$$

At semi-infinite interval $x > 0$, only the solution with negative $\kappa = \kappa_-$ does not diverge at infinity. Given the Laplace-transformed concentration at the inlet, $\tilde{C}(0, p)$, we obtain

$$\tilde{C}(x, p) = \tilde{C}(0, p) \exp \left(\frac{x}{2\lambda} - x \left[\frac{1}{4\lambda^2} + \frac{p}{\lambda v} \right]^{1/2} \right). \tag{3.5}$$

The inverse Laplace transformation of the above equation is a convolution,

$$C(x, t) = \int_0^t dt' \, C(0, t - t') \, g(x, t'), \tag{3.6}$$

with the tracer Green's function (GF)

$$g(x, t) = \frac{x}{2(\pi \lambda v)^{1/2}} \frac{1}{t^{3/2}} \exp \left(-\frac{(x - vt)^2}{4\lambda vt} \right). \tag{3.7}$$

In the special case $C(0, t) = C_0 =$const, the integration results

$$C = \frac{C_0}{2} \left(1 + \text{erf} \left[\frac{tv - x}{2(tv\lambda)^{1/2}} \right] + e^{x/\lambda} \, \text{erfc} \left[\frac{tv + x}{2(tv\lambda)^{1/2}} \right] \right), \tag{3.8}$$

where $\text{erfc}(z) \equiv 1 - \text{erf}(z)$ is the complementary error function.

We note that the spatial derivative of the solution of Eq. (3.8) at $x = 0$ is different from zero. Indeed, it depends on time and is divergent at small t, implying an unphysically

large diffusive component of the particle current,

$$C'(0,t) = \frac{C_0}{2}\left(\frac{\operatorname{erfc}(\alpha)}{2\lambda} - \frac{e^{-\alpha^2}}{(\pi t v \lambda)^{1/2}}\right), \quad \alpha^2 \equiv \frac{tv}{4\lambda}. \tag{3.9}$$

In the presence of the straining term, $r_d = A_0 N_0 C$ in Eq. (3.1), the GF can be obtained from Eq. (3.7) by introducing exponential decay with the rate $A_0 N_0$,

$$g(x,t) = \frac{x}{2(\pi\lambda v)^{1/2}} \frac{e^{-A_0 N_0 t}}{t^{3/2}} \exp\left(-\frac{(x-vt)^2}{4\lambda v t}\right). \tag{3.10}$$

Note that we wrote the straining rate as a product of the capture rate A_0 by infinite-capacity "permanent" traps with the concentration N_0 per unit volume of water. Such a factorization is convenient for the non-linear model presented later in Sec. 3.4. The same notations are employed throughout this work for consistency.

3.3 Linearized mean-field filtration model

In this section we discuss the linearized convection-only multitrap filtration model, a variant of the multirate CDE model first proposed in Ref. [61]. Our model is characterized by a (possibly continuous) density of traps as a function of detachment rate [see Eq. (3.23)]. Generically, continuous trap distribution leads to non-exponential (e.g., power-law) asymptotic forms of the concentration in the effluent on the washout stage.

The main purpose of this section is to demonstrate that "shallow" traps with large detachment rates have the same effect as the hydrodynamic dispersivity in CDE. In addition, the obtained exact solutions will be used in Sec. 3.4 as a basis for the analysis of the full non-linear mean-field model for filtration under unfavorable conditions.

34

3.3.1 Shallow traps as a substitute for diffusion

To rectify the problems with the diffusion approximation noted previously, we suggest an alternative approach for the propagation of particles through the filtering medium. Instead of considering the drift with an average velocity with symmetric diffusion-like deviations accounting for dispersion of individual trajectories, we consider the convective motion with the maximum velocity v. The random twists and turns delaying the individual trajectories are accounted for by introducing Poissonian traps which slow down the passage of the majority of the particles through the column. In the simplest case suitable for tracer particles, the relevant kinetic equations read as follows:

$$\dot{C} + vC' + N_1\dot{n}_1 = 0, \quad \dot{n}_1 = A_1C - B_1n_1, \tag{3.11}$$

with $n_1 \equiv n_1(x, t)$ as the auxiliary variable describing the average number of particles in a trap, N_1 as the number of traps per unit water volume, A_1 as the trapping rate, and B_1 as the release rate. The particular normalization of the coefficients is chosen to simplify the formulation of models with traps subject to saturation in Sec. 3.4.

To simulate dispersivity where all time scales are inversely proportional to propagation velocity, we must choose both A_1 and B_1 proportional to v. The corresponding parameter σ in $A_1 \equiv \sigma v$ has a dimension of area and can be viewed as a trapping cross section. The length ℓ in the release rate $B_1 \equiv v/\ell$ can be viewed as a characteristic size of a stagnation region. On general grounds we expect $\sigma \propto \ell^2$ with ℓ on the order of the grain size.

3.3.2 Single-trap model with straining.

To illustrate how shallow traps can provide for dispersivity in convection-only models, let us construct the exact solution of Eq. (3.11). In fact, it is convenient to consider a slightly

generalized model with the addition of straining,

$$\dot{C} + vC' + N_1\dot{n}_1 = -A_0 N_0 C, \quad \dot{n}_1 = A_1 C - B_1 n_1. \tag{3.12}$$

With zero initial conditions the Laplace transformation gives for $\tilde{C} \equiv \tilde{C}(x,p)$,

$$\left(p + A_0 N_0 + \frac{A_1 N_1 p}{p + B_1} \right) \tilde{C} + v\tilde{C}' = 0. \tag{3.13}$$

The boundary value for Laplace-transformed $C(x,t)$ at the inlet is given by $\tilde{C}(0,p)$. With initially clean filter, $C(x,0) = n(x,0) = 0$, and a given free particle concentration $C(0,t)$ at the inlet, the solution to the linear one-trap convection-only model with straining [Eq. (3.12)] is a convolution of the form presented in Eq. (3.6) with the following GF [62]:

$$
\begin{aligned}
g(x,t) \;=\; & e^{-\beta x/v - B_1(t-x/v)} \Bigg\{ \delta\left(t - x/v\right) \\
& + \theta(t - x/v)\frac{(A_1 N_1 B_1 x)^{1/2}}{(tv - x)^{1/2}} I_1(\zeta_t) \Bigg\},
\end{aligned}
\tag{3.14}
$$

where $\beta \equiv A_0 N_0 + A_1 N_1$ is the clean-bed trapping rate, $\theta(z)$ is the Heaviside step-function, and $I_1(\zeta_t)$ is the modified Bessel function of the first kind with the argument

$$\zeta_t \equiv \frac{2}{v}\left[A_1 N_1 B_1 (tv - x)x \right]^{1/2}. \tag{3.15}$$

The singular term with the δ function $\delta(t - x/v)$ in Eq. (3.14) represents the particles at the leading edge which propagate freely with the maximum velocity v without ever being trapped. The corresponding weight $\exp(-\beta x/v)$ decreases exponentially with the distance from the origin.

Sufficiently far from both the origin and from the leading edge, where the argument

ζ_t [Eq. (3.15)] of the Bessel function is large, we can use the asymptotic form,

$$I_1(\zeta) = \frac{1}{(2\pi\zeta)^{1/2}} e^{\zeta} \left[1 + \mathcal{O}(\zeta^{-1}) \right], \operatorname{Re} \zeta > 0. \tag{3.16}$$

Subsequently, Eq. (3.14) becomes

$$g(x,t) \approx e^{-A_0 N_0 x/v} \frac{B_1 \xi^{1/4}}{2\pi^{1/2} \tau^{3/4}} \exp -(\sqrt{\xi} - \sqrt{\tau})^2, \tag{3.17}$$

where $\tau \equiv B_1(t - x/v)$ is the dimensionless retarded time in units of the release rate, and $\xi \equiv A_1 N_1 x/v$ is the dimensionless distance from the origin in units of the trapping mean free path.

The correspondence with the GF in Eq. (3.10) for the CDE with linear straining [or Eq. (3.7) for the CDE tracer model in the case of no permanent traps, $N_0 = 0$] can be recovered from Eq. (3.17) by expanding the square roots in the exponent around its maximum at $\xi = \tau$, or $x = v_0 t$, with the effective velocity $v_0 = vB_1/(B_1 + N_1 A_1)$. Specifically, suppressing the prefactor due to straining, [$N_0 = 0$ in Eq. (3.17)], we obtain for the asymptotic form of the exponent at large t,

$$g(x,t) \propto \exp -\frac{(x - v_0 t)^2}{4\lambda_0 v_0 t}, \tag{3.18}$$

with the effective dispersivity coefficient [cf. Eq. (3.7)]

$$\lambda_0 = v \frac{N_1 A_1}{(N_1 A_1 + B_1)^2}. \tag{3.19}$$

The approximation is expected to be good as long as both x and t are large compared to the width of the bell-shaped maximum.

The actual shapes of the corresponding GFs, Eqs. (3.7) and (3.14) in the absence of

permanent traps, $N_0 = 0$, are compared in Fig. 3.2. While the shape differences are substantial at small t, they disappear almost entirely at later times.
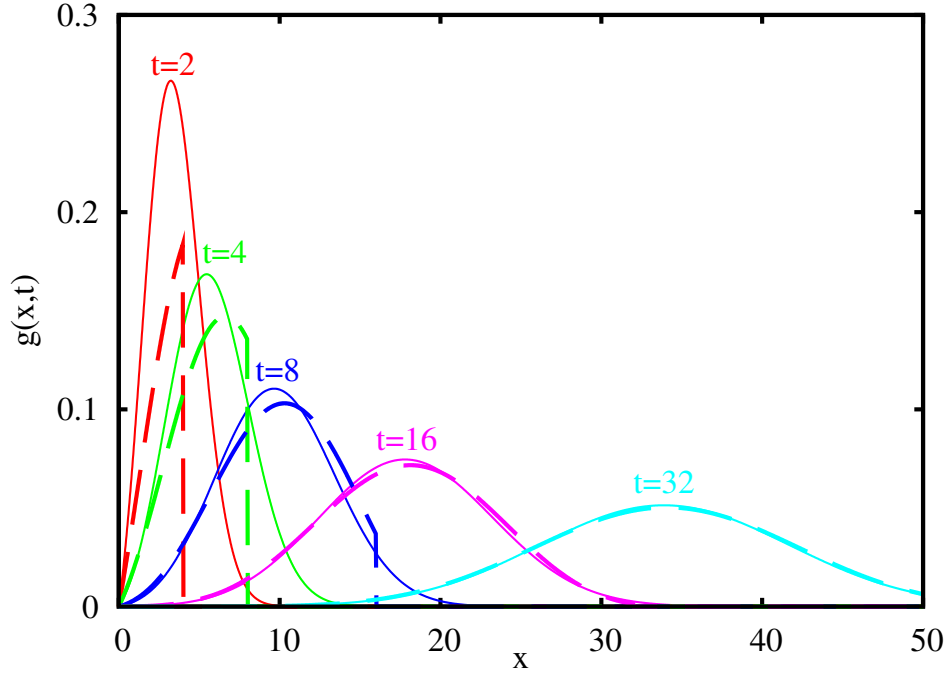

Figure 3.2: (Color online) Comparison of the spatial dependence of the GFs for the tracer model implemented as the convection-diffusion equation [Eq. (3.1)] with $r_d = 0$ (solid lines) and the single-trap convection model [Eq. (3.11)] (dashed lines). Specifically, we plot Eq. (3.7) and the regular part of Eq. (3.14) with $N_0 = 0$, using identical values of $v = v_0 = 1$ and $\lambda = \lambda_0 = 1$ and the release rate $B_1 = 1/2$ (half the maximum value at these parameters) at $t = 2, 4, 8, 16, 32$. Once the maximum is sufficiently far from the origin, the two GFs are virtually identical (see Sec. 3.3.2).

3.3.3 Multitrap convection-only model

Even though the solutions of the single-trap model correspond to those of the CDE [Eq. (3.2)], the model presented in Eq. (3.12) is clearly too simple to accurately describe filtration under conditions where trapped particles can be subsequently released. At the very least, in addition to straining and "shallow" traps that account for the dispersivity, describing the experiments[51, 52] requires another set of "deeper" traps with a smaller release rate.

More generally, consider a linear model with m types of traps differing by the rate

coefficients A_i, B_i,

$$\dot{C} + vC' + \sum_{i=1}^{m} N_i \dot{n}_i = 0, \quad \dot{n}_i = A_i C - B_i n_i. \tag{3.20}$$

The corresponding solution can be obtained in quadratures in terms of the Laplace transformation. With the initial condition, $C(x,0) = n_i(x,0) = 0$ and a given time-dependent concentration at the inlet, $C(0,t) = C_0(t)$, the result for $C(x,t)$ is a convolution of the form presented in Eq. (3.6) with the GF given by the inverse Laplace transformation formula,

$$g(x,t) = \int_{c-i\infty}^{c+i\infty} \frac{dp}{2\pi i} e^{p[t - x/v - x\Sigma(p)/v]}, \tag{3.21}$$

with the response function

$$\Sigma(p) \equiv \sum_{i=1}^{m} \frac{A_i N_i}{p + B_i} = \int \frac{dB\, \rho(B)}{p + B}. \tag{3.22}$$

Here we introduced the effective density of traps,

$$\rho(B) \equiv \sum_{i=1}^{m} A_i N_i \delta(B - B_i), \tag{3.23}$$

corresponding to various release rates.

The general structure of the concentration profile can be read off directly from Eq. (3.21). It gives zero for $t < x/v$, consistent with the fact that v is the maximum propagation velocity in Eq. (3.20). The structure of the leading-edge singularity (the amplitude of the δ function due to particles which never got trapped) is determined by the large-p asymptotics of the integrand in

Eq. (3.21). Specifically, GF (3.21) can be written as

$$g(x,t) = e^{-\beta x/v}\delta(t - x/v) + \theta(t - x/v)g_{\text{reg}}(x,t), \qquad (3.24)$$

where $\beta = \lim_{p\to\infty} p\Sigma(p) = \sum_i N_i A_i$ [cf. Eq. (3.14)] is the clean-bed trapping rate, and g_{reg} is the non-singular part of the GF.

Similarly, the structure of the diffusion-like peak of the GF away from both the origin and the leading edge is determined by the saddle point of the integrand in Eq. (3.21) at small p. Assuming the expansion $\Sigma(p) = \Sigma(0) - \Sigma_1 p + \mathcal{O}(p^2)$ and evaluating the resulting Gaussian integral around the saddle point at

$$p_\star \approx \frac{t - x/v_0}{2x\Sigma_1/v}, \qquad v_0 \equiv \frac{v}{1 + \Sigma(0)}, \qquad (3.25)$$

we obtain

$$g(x,t) \approx \frac{1}{2(\pi\Sigma_1 x/v)^{1/2}} e^{-(t-x/v_0)^2/(4\Sigma_1 x/v)}. \qquad (3.26)$$

The exponent near the maximum can be approximately rewritten in the form of that in Eq. (3.7), with the effective dispersivity

$$\lambda_0 = \frac{v_0^2}{v}\Sigma_1 = \frac{v\Sigma_1}{[1 + \Sigma(0)]^2}. \qquad (3.27)$$

For the case of one trap, $m = 1$, the expressions for the effective parameters clearly correspond to our earlier results of Eqs. (3.18) and (3.19). Note that the precise structure of the exponent and the prefactor in Eq. (3.26) is different from those in Eq. (3.18) which was obtained by a more accurate calculation.

The effective diffusion approximation [Eq. (3.26)] is accurate for large x near the max-

imum as long as the integral in Eq. (3.21) remains dominated by the saddle-point in Eq. (3.25). In particular, the poles of response function (3.22) must be far from $p_\star$. This is easily satisfied in the case of "shallow" traps with large release rates $B_i \gg |p_\star|$.

On the other hand, this condition could be simply violated in the presence of "deep" traps with relatively small B_i. Over small time intervals compared to the typical dwell time B_i^{-1}, these traps may work in the straining regime in which they would *not* contribute to the effective dispersivity. This situation may be manifested as an apparent time-dependence of the effective drift velocity v_0 and/or the dispersivity λ_0.

3.3.4 Model with a continuous trap distribution

The multitrap generalization given in Eq. (3.20) for filtration is clearly a step in the right direction if we want an accurate description of the filtering experiments.

Indeed, apart from the special case of a regular array of identical densely-packed spheres with highly polished surfaces, one expects the trapping sites (e.g., the contact points of neighboring grains) to differ. For small particles such as viruses, even a relatively small variation in trapping energy could result in a wide range of release rates B_i differing by many orders of magnitude[56, 53]. Under such circumstances, it is appropriate to consider mean-field models with continuous trap distributions.

Here we only consider a special case of a continuous distribution of the trap parameters, A_i and B_i, such that the release-rate density in Eq. (3.22) has an inverse-square-root singularity, $\rho(B) = \rho_{1/2}/(\pi B^{1/2})$, with the release rates ranging from infinity all the way to zero. The corresponding response function (3.22) could be expressed as

$$\Sigma(p) = \rho_{1/2}/p^{1/2}. \tag{3.28}$$

The inverse Laplace transform [Eq. (3.21)] gives the following GF:

$$g(x,t) = \frac{x\rho_{1/2}}{2\sqrt{\pi}v\tau^{3/2}} e^{-x^2\rho_{1/2}^2/(4v^2\tau)}\theta(\tau), \quad \tau \equiv t - \frac{x}{v}. \tag{3.29}$$

Note that, in accordance with Eq. (3.24), there is no leading-edge δ function near $t = x/v$ as the expression for the corresponding trapping rate β diverges. Because of the singular behavior of $\Sigma(p)$ at $p = 0$, there is no saddle-point expansion of the form given in Eq. (3.25). Thus, there is no Gaussian representation analogous to Eq. (3.26): at large t, the maximum of the GF is located at $x_{\max} = v\rho_{1/2}(2t)^{1/2}$, which is also of the order of the width of the Gaussian maximum. The GF [Eq. (3.29)] for two representative values of $\rho_{1/2}$ is plotted in Fig. 3.3.
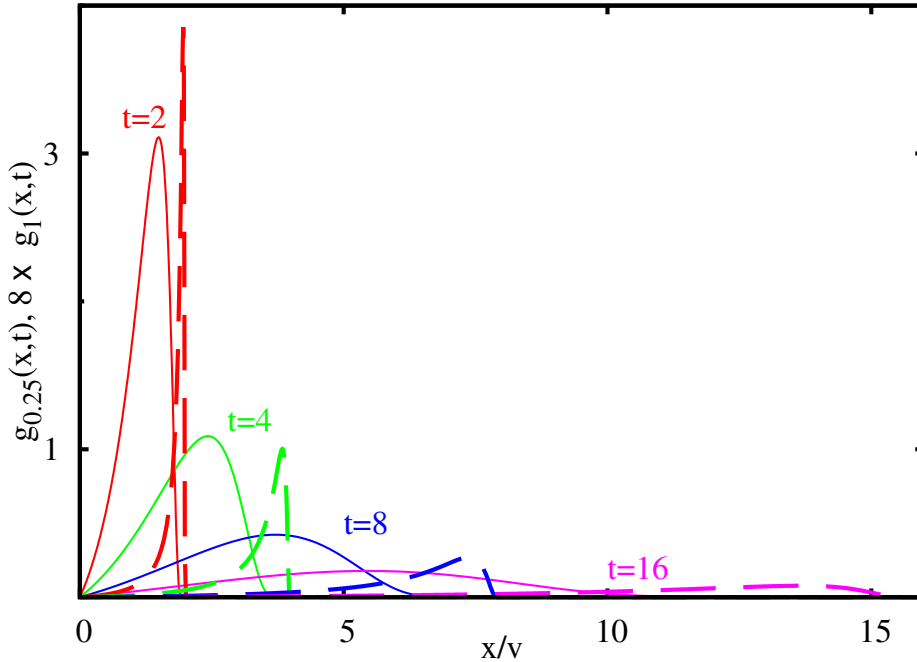
Figure 3.3: (Color online) Spatial dependence of the GF [Eq. (3.29)] for the model presented in Eq. (3.20) with continuous distribution of trap parameters corresponding to inverse-square-root singularity in the response function [see Eqs. (3.22) and (3.28))]. Dashed lines show the GF at $\rho_{1/2} = 0.25$, while solid lines present the same GF at $\rho_{1/2} = 1$ multiplied by the factor of 8. We chose $t = 2, 4, 8, 12$ as indicated in the plot. Unlike in Fig. 3.2, due to abundance of traps with long release time, the GFs do not asymptotically converge toward a Gaussian form.

We also note that for large t at any given x, Eq. (3.29) has a power-law tail $\propto t^{-3/2}$.

This property is generic for continuous trap density distributions leading to small-p power-law singularities in $\Sigma(p)$. For example, taking the density of the release rates as a power law in B,

$$\rho(B) = \frac{\sin(\pi s)}{\pi} \frac{\rho_s}{B^s}, \qquad (3.30)$$

where s is the corresponding exponent, $0 < s < 1$, we obtain $\Sigma(p) = \rho_s p^{-s}$, and the large-$t$ asymptotic of the GF at a fixed finite x scales as

$$g(x,t) \propto t^{s-2}. \qquad (3.31)$$

Such a power law is an essential feature of continuous distribution (3.30) of the detachments rates; it cannot be reproduced by a discrete set of rates B_i which always produce an *exponential* tail.

3.4 Filtration under unfavorable conditions

3.4.1 Multitrap model with saturation

The considered linearized filtration model presented by Eq. (3.20) can be used to analyze filtration of identical particles in small concentrations and over limited time interval as long as the trapped particles do not affect the filter performance. However, unless the model is used to simulate tracer particle dynamics in which no actual trapping occurs, it is unlikely that the model remains valid as the number of trapped particles grows.

Indeed, one expects that a trapped particle changes substantially the probability for subsequent particles to be trapped in its vicinity. Under *favorable* filtering conditions characterized by filter ripening [63, 64], the probability of subsequent particle trapping *increases* with time as the number of trapped particles n_i grows. On the other hand, under *unfavorable* filtering

conditions, where the Debye screening length is large compared to the trap size ℓ, for charged particles one expects trapping probabilities $A_i(n_i)$ to *decrease* with n_i.

If repulsive force between particles is large, we can assume that only one particle is allowed to be captured in each trap. Subsequently, a single trap can be characterized by an attachment rate A_i when it is empty and a detachment rate B_i when it is occupied, and the mean-field trapping/release dynamics for a given group of trapping sites can be written as

$$\dot{n}_i = C\,A_i(1 - n_i) - B_i n_i. \tag{3.32}$$

Note that this equation is non-linear because it contains the product of Cn_i.

Previously, similar filtering dynamics was considered in a number of publications (see Refs. [51] and [52] and references therein). In the present work, we allow for a possibility of groups of traps differing by the rate parameters A_i and B_i. The distribution of rate parameters can also be viewed as an analytical alternative of the computer-based models describing a network of pores of varying diameter[54, 56, 57].

Our mean-field transport model is completed by adding the kinetic equation for the motion of free particles with concentration C,

$$\dot{C} + vC' + \sum_{i=1}^{m} N_i \dot{n}_i = 0, \tag{3.33}$$

which has the same form as the linearized equations [Eq. (3.20)] considered in Sec. 3.3.4.

We note that for shallow traps with large release rates B_i, the non-linearity inherent in Eq. (3.32) is not important for sufficiently small suspended particle concentrations C. Indeed,

if C is independent of time, the solution of Eq. (3.32) saturates at

$$n_i(C) = \frac{CA_i}{B_i + CA_i}.$$

(3.34)

For small free-particle concentration C, or for any C and large enough B_i, the trap population is small compared to 1, and the non-linear term in Eq. (3.32) can be ignored.

Therefore, as discussed in relation with the linearized multitrap model [see Sec. 3.3A and Eq. (3.20)], the effect of shallow traps is to introduce dispersivity of the arrival times of the particles on different trajectories. For this reason, we are free to drop the dispersivity term [cf. the CDE model, Eq. (3.1)], and use a simpler convection-only model (3.33) with several groups of traps with density N_i per unit water volume, characterized by the relaxation parameters A_i and B_i.

3.4.2 General properties: Stable filtering front

The constructed non-linear equations [Eqs. (3.32) and (3.33)] describe complicated dynamics which is difficult to understand in general. Here, we introduce the front velocity, a parameter that characterizes the speed of deterioration of the filtering capacity.

Consider a semi-infinite filter, with the filtering medium initially clean, and the concentration $C(0,t) = C_A$ of suspended particles at the inlet constant. After some time, the concentration of deposited particles near the inlet reaches the dynamical equilibrium $n_i(C_A)$ [Eq. (3.34)] and, on average, the particles will no longer be deposited there. At a given inlet concentration, the filtering medium near the inlet is saturated with deposited particles. On the other hand, sufficiently far from the inlet, the filter is still clean. On general grounds, there should be some crossover between these two regions.

The size of the saturated region grows with time [see Fig. 3.4]. The corresponding

45

front velocity $v_A \equiv v(C_A)$ can be easily calculated from the particle balance equation,

$$v_A C_A + v_A \sum_i N_i n_i(C_A) = v C_A. \tag{3.35}$$

This equation balances the number of additional particles needed to increase the saturated region by $\delta x = v_A \delta t$ on the left, with the number of particles brought from the inlet on the right [see Fig. 3.4]. The same equation can also be derived if we set $C = C(x - v_A t)$, $n_i = n_i(x - v_A t)$ and integrate Eq. (3.33) over the entire crossover region. The trapped particle density saturates as given by Eq. (3.34), and the resulting front velocity is

$$v(C_A) = \cfrac{v}{1 + \sum_i \cfrac{N_i A_i}{A_i C_A + B_i}}. \tag{3.36}$$

This is a monotonously increasing function of C_A: larger inlet concentration C_A leads to higher front velocity, which implies that the filtering front is stable with respect to perturbations. Indeed, in Appendix we show that the velocity v_{AB} of a secondary filtering front with the inlet concentration $C_B > C_A$ (see Fig. 3.5), moving on the background of equilibrium concentration of free particles C_A, is higher than v_A, i.e., $v_{AB} > v_A$. Thus, if for some reason the original filtering front is split into two parts, moving with the velocities v_A and v_{AB}, the secondary front will eventually catch up, restoring the overall front shape.

We emphasize that the existence of the stable filtering front is in sharp contrast with the linearized filtering problem [see Eq. (3.20)], where the propagation velocity v_0 [Eq. (3.25)] is independent of the inlet concentration, and any structure is eventually washed out dispersively (the width of long-time GF does not saturate with time). Also, in the case of the filter ripening, the nonlinear term in Eq. (3.32) will be negative and thus would prohibit the filtering front
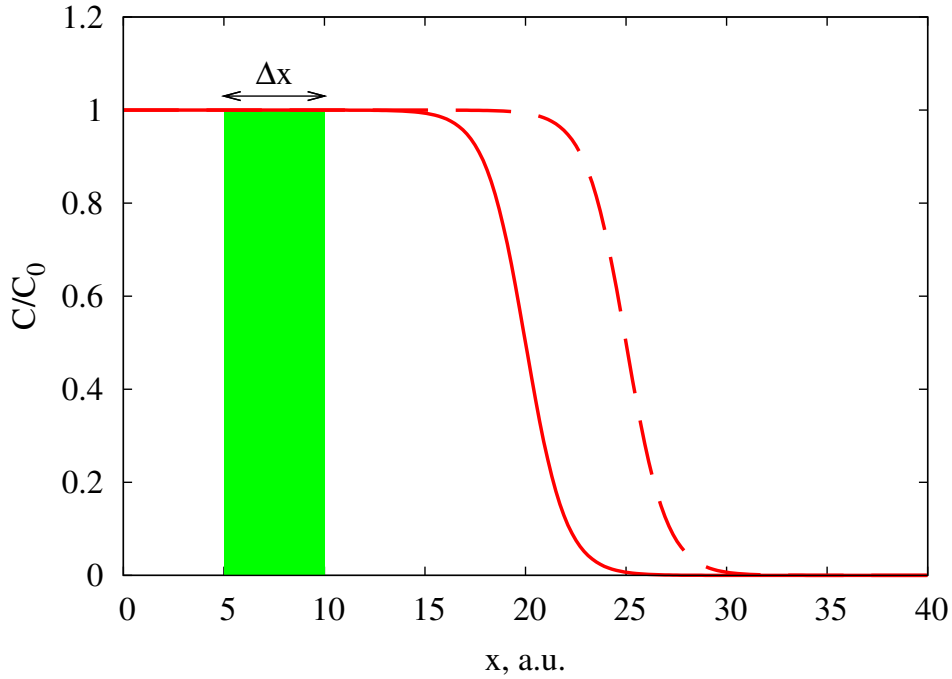
Figure 3.4: Solid line shows the free particle concentration near a filtering front. Dashed line shows the front shifted by Δx; the additional free and trapped particles in the shaded region are brought from the inlet [see Eq. (3.35)]. See Eq. (3.52) for exact front shape.

solutions due to the fact that the secondary fronts move slower, $v_{AB} < v_A$. The non-linear problem with saturation is thus somewhat analogous to Korteweg-de Vries solitons where the dispersion and nonlinearity compete to stabilize the profile[65, 66].

3.4.3 Exactly solvable case

3.4.3.1 General solution

Compared to the linear case presented in Sec. 3.3, the physics behind the non-linear equations [Eqs. (3.32) and (3.33)] is much more complicated. However, the structure of these equations immediately indicates that non-linearity reduces filtering capacity because trapping sites could saturate in this model [see Eq. (3.34)]. While the relevant equations can also be solved numerically, a thorough understanding of the filtering system, especially with large or infinite number of traps, is difficult to achieve.
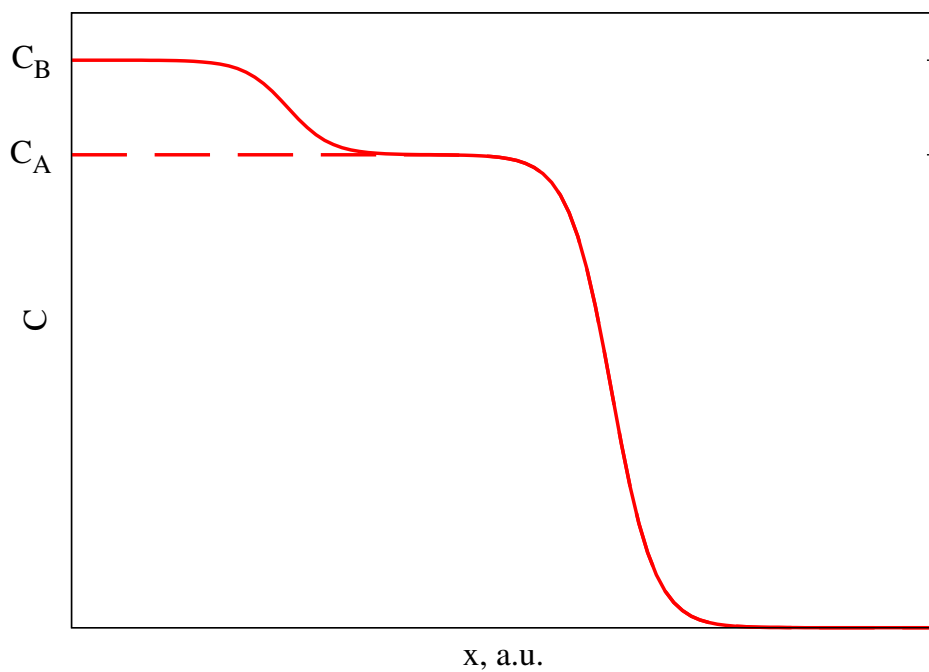
Figure 3.5: Free particle concentration $C(x, t)$ with two filtering fronts. The initial front moves on the background of clean filter and leaves behind the equilibrium filtering medium with $C = C_A$. The secondary front with higher inlet concentration C_B is moving on partially saturated medium. With nonlinearity as in Eq. (3.32), the secondary front is always faster, $v_{AB} > v_A$; the two fronts will eventually coalesce into a single front.

To gain some insight about the role of the different parameters in the filtering process, we specifically focus on the non-linear models presented by Eqs. (3.32) and (3.33) which can be rendered into a linear set of equations, very similar to the linear multitrap model [Eq. (3.20)]. To this end, we consider the case where all trapping sites have the same trapping cross sections, that is, all $A_i = A$ in Eq. (3.32). If we introduce the time integral

$$u(x,t) \equiv \int_0^t C(x,t')dt', \tag{3.37}$$

then Eq. (3.32) after a multiplication by $\exp Au$ can be written as

$$\partial_t \left(n_i e^{Au} \right) + B_i \left(n_i e^{Au} \right) = \partial_t \left(e^{Au} \right). \tag{3.38}$$

Clearly, these are a set of linear equations,

$$\dot{a}_i + B_i a_i = \dot{w}, \tag{3.39}$$

with the following variables

$$w \equiv w(x,t) = e^{Au}, \quad a_i \equiv a_i(x,t) = n_i w. \tag{3.40}$$

Note that Eq. (3.33) can also be written as a set of linear equations in terms of these variables. If we integrate Eq. (3.33) over time, we find

$$\dot{u} + vu' + \sum_{i=1}^m N_i n_i = 0, \tag{3.41}$$

where we assumed initially clean filter, $C(x,0) = n_i(x,0) = 0$. Considering that $\dot{w} = A\dot{u}\,w$

and $w' = Au'\,w$, we obtain

$$\dot{w} + vw' + A \sum_{i=1}^{m} N_i a_i = 0. \tag{3.42}$$

The main difference of the linear Eqs. (3.39) and (3.42) from Eqs. (3.20) is in their initial and boundary conditions,

$$w(x,0) = 1, \quad a_i(x,0) = 0, \tag{3.43}$$

$$w(0,t) = e^{Au_0(t)}, \quad u_0(t) \equiv \int_0^t dt'\, C(0,t'). \tag{3.44}$$

Note that with the time-independent concentration of the particles in suspension at the inlet, i.e., $C(0,t) = C_0$, boundary condition (3.44) gives a growing exponent,

$$w_0(t) \equiv w(0,t) = e^{AC_0 t}. \tag{3.45}$$

The derived equations can be solved with the use of the Laplace transformation. Denoting $\tilde{w} \equiv \tilde{w}(x,p) = \mathcal{L}_p\{w(t)\}$ and eliminating the Laplace-transformed trap populations $\tilde{n}_i(x,p) \equiv \mathcal{L}_p\{n_i(x,t)\}$, we obtain

$$(p\tilde{w} - 1)\left[1 + \Sigma(p)\right] + v\tilde{w}' = 0, \quad \Sigma(p) \equiv A \sum_i \frac{N_i}{p + B_i}. \tag{3.46}$$

The response function $\Sigma(p)$ is identical to that in Eq. (3.22), and for the case of continuous trap distribution we can also introduce the effective density of traps, $\rho(B) \equiv A \sum_i N_i \delta(B - B_i)$. The solution of Eq. (3.46) and the Laplace-transformed boundary condition [Eq. (3.44)] becomes

$$\tilde{w} = \frac{1}{p} + \left[\tilde{w}_0(p) - \frac{1}{p}\right] e^{-[1+\Sigma(p)]px/v}, \tag{3.47}$$

where $\tilde{w}(0, p) = \tilde{w}_0(p)$. Employing the same notation as in Eq. (3.21), the real-time solution of Eqs. (3.39) and (3.42) with the boundary conditions [Eqs. (3.43) and (3.44)] can be written in quadratures,

$$w(x, t) = 1 + \int_0^t dt' \ [w_0(t - t') - 1] \ g(x, t'). \tag{3.48}$$

The time-dependent concentration can be restored from here with the help of logarithmic derivative,

$$C(x, t) = \frac{1}{A} \frac{\partial \ln w(x, t)}{\partial t}. \tag{3.49}$$

3.4.3.2   Structure of the filtering front

In the special case $C(0, t) = C_0 = \text{const}$, the integrated concentration [Eq. (3.37)] is linear in time at the inlet, $u_0(t) = C_0 t$, and $w(0, t)$ grows exponentially [see Eq. (3.45)]. This exponent determines the main contribution to the integral in Eq. (3.48) for large t and x. Indeed, in this case we can rewrite Eq. (3.48) exactly as $w(x, t) = 1 + J(C_0) - J(0)$, where

$$J(C_0) \equiv e^{AC_0 t} \int_0^t dt' \ e^{-AC_0 t'} g(x, t'). \tag{3.50}$$

Note that $J(0)$ is proportional to the solution of the linearized equations [Eq. (3.20)] with time-independent inlet concentration $C(0, t) = \text{const}$ [see Eq. (3.6)]. The corresponding front is moving with the velocity v_0 [Eq. (3.25)] and is widening over time [Eqs. (3.26) and (3.27)]. Thus, for $x/v_0 - t$ positive and sufficiently large, this contribution to $w(x, t)$ is small and can be ignored. In the opposite limit of large negative $x/v_0 - t$, $J(0) = 1$, which exactly cancels the first term in Eq. (3.48).

On the other hand, the term $J(C_0)$ grows exponentially large with time. At large enough t, the integration limit can be extended to infinity, and the integration in Eq. (3.50)

becomes a Laplace transformation, thus

$$
\begin{aligned}
w(x,t) &\approx 1 + e^{AC_0 t} \int_0^\infty dt'\, e^{-AC_0 t'} g(x,t') \\
&= 1 + e^{p_0 t}\, e^{-[1+\Sigma(p_0)]p_0 x/v}, \quad p_0 \equiv AC_0.
\end{aligned}
\tag{3.51}
$$

This results in the following free-particle concentration [see Eq. (3.49)],

$$
C(x,t) = \frac{C_0}{e^{[x/v(C_0)-t]AC_0} + 1},
\tag{3.52}
$$

and the occupation of the ith trap [Eqs. (3.39) and (3.40)],

$$
n_i(x,t) = \frac{A}{B_i + AC_0} C(x,t),
\tag{3.53}
$$

with the front velocity

$$
v(C_0) \equiv \frac{v}{1 + \Sigma(AC_0)}.
\tag{3.54}
$$

Note that this coincides exactly with the general case presented in Eq. (3.36) if we set all $A_i = A$.

3.4.3.3   Filtering front formation

The approximation in Eq. (3.51) is valid in the vicinity of the front, $|x/v(C_0) - t| \lesssim (AC_0)^{-1}$, as long as $x/v_0 - t$ is positive and large. Since $v(C_0) > v_0 = v(0)$, this implies

$$
x\left[\frac{1}{v_0} - \frac{1}{v(C_0)}\right] \gg \frac{1}{AC_0},
\tag{3.55}
$$

which provides an estimate of the distance from the outlet where the front structure [Eqs. (3.52) and (3.53)] is formed. The exactness of the obtained asymptotic front structure can be verified

directly by substituting the obtained profiles in Eqs. (3.32) and (3.33).

The exact expressions in Eqs. (3.48) and (3.49) for the free-particle concentration can be integrated completely in some special cases. Here we list two such results and demonstrate the presence of striking similarities in the profiles $C(x, t)$ between different models, despite their very different rate distributions. Furthermore, we show that the corresponding exact solutions [Eq. (3.49)] converge rapidly toward the general filtering front [Eq. (3.52)].

Single-trap model with straining. In Sec. 3.3.2, we found the explicit expression [Eq. (3.14)] for the GF in the case of the linear model for two types of trapping sites with rates A_1 and B_1 and permanent sites with the capture rate A_0. The resulting GF (with $A_1 = A_0 = A$ and $B_1 = B$) can be used in Eq. (3.48) to construct the solution for the corresponding model with saturation,

$$\dot{C} + vC' + N_0\dot{n}_0 + N_1\dot{n}_1 = 0, \tag{3.56}$$

$$\dot{n}_0 = AC(1 - n_0), \quad \dot{n}_1 = AC(1 - n_1) - B_1 n_1. \tag{3.57}$$

Let us consider the special case of the inlet concentration, $C(0, t) = C_0\,\theta(T - t)\,\theta(t)$, constant over the interval $0 < t < T$, and zero afterwards. The function $w_0(t)$ [see Eq. (3.44)] is, then

$$w_0(t) = \exp[AC_0\min(t, T)], \tag{3.58}$$

and the integration in Eq. (3.48) gives

$$w = 1 + e^{-\beta\xi}\left[W(t) - e^{AC_0T}W(t - T)\right], \tag{3.59}$$

$$W(t) \equiv \theta(t - \xi)\Big\{\left[e^{AC_0(t-\xi)} - 1\right]$$
$$+ \int_\xi^t d\tau\, e^{-B_1(\tau-\xi)}\left[e^{AC_0(t-\tau)} - 1\right]\frac{d}{d\tau}I_0(\zeta_\tau)\Big\}, \tag{3.60}$$

where $\xi \equiv x/v$ and ζ_τ is given in Eq. (3.15). The concentration of free particles, $C(x, t)$, can be now obtained through Eq. (3.49). The step function $\theta(t - x/v)$ included in w indicates that it takes at least $t = x/v$ for a particle to travel a distance x.

Figure 3.6 illustrates $C(x, t)$ as a function of distance, x, at a set of discrete values of time $t = 1, 2, \ldots, 16$. The model parameters as indicated in the caption were obtained by fitting the response function $\Sigma(p) = AN_0/p + AN_1/(p + B_1)$ at the interval $0.5 < p < 5.0$ to that of the model with the continuous trap distribution (see Fig. 3.7). The solid lines show the curves for $t \leq T$, while the dashed lines correspond to $t > T$; they have a drop in the concentration near the origin consistent with the boundary condition at the inlet. The exact profiles show excellent convergence toward the corresponding front profiles computed using Eq. (3.52) (symbols).
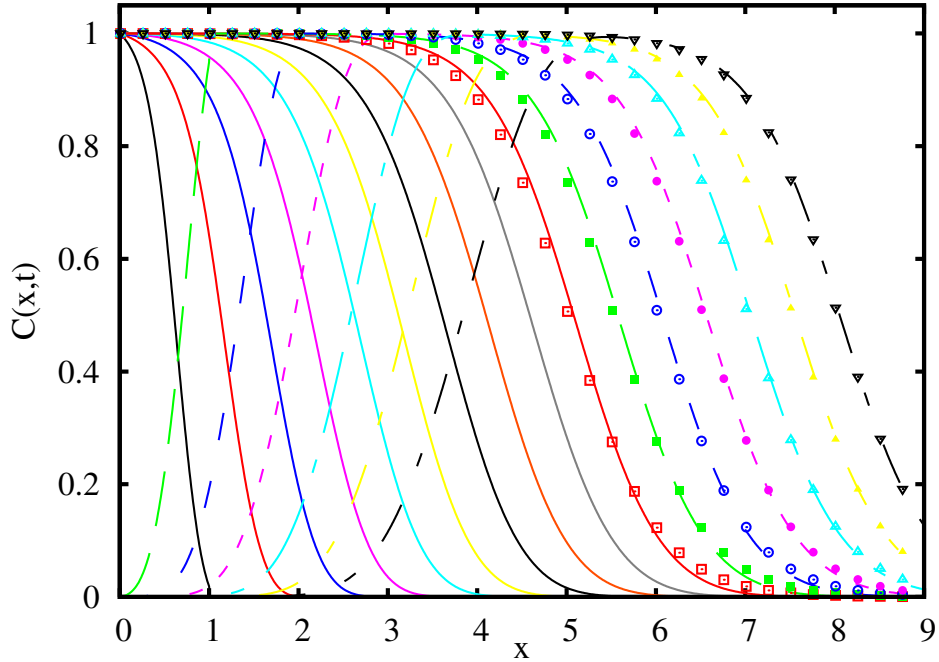
Figure 3.6: (Color online) Formation of the filtering front for the single-trap filtering model with straining [Eq. (3.56)]. Lines show the free-particle concentration $C(x, t)$ extracted from Eq. (3.56) with $T = 10$, $A = v = C_0 = 1$, $N_0 = 0.388$, $N_1 = 3.60$, and $B_1 = 4.97$, for $t = 1, 2, \ldots, 16$. Symbols show the front solution [Eq. (3.52)] for $t \geq 10$ with the front velocity [Eq. (3.54)].

Model with square-root singularity. Let us now consider the non-linear model, [Eqs. (3.33)

and (3.32)] with the inverse-square-root continuous trap distribution, producing the response function given in Eq. (3.28). The model is exactly solvable if we set all $A_i = A$, while allowing the trap densities N_i vary with B appropriately.

The solution for the auxiliary function w corresponding to the inlet concentration $C(0, t)$ constant on an interval of duration T is obtained by combining Eqs. (3.48) and (3.58), with the relevant GF [Eq. (3.29)]. The resulting x-dependent curves $C(x, t)$ at a set of discrete time values are shown in Fig. (3.7), along with the corresponding asymptotic front profiles (symbols), for a parameter set as indicated in the caption. The solid lines show the curves for $t \leq T$. The dashed lines are for $t > T$; they display a drop of the concentration near the origin consistent with the boundary condition at the inlet. Again, the time-dependent profiles show gradual convergence toward front solution (3.52).
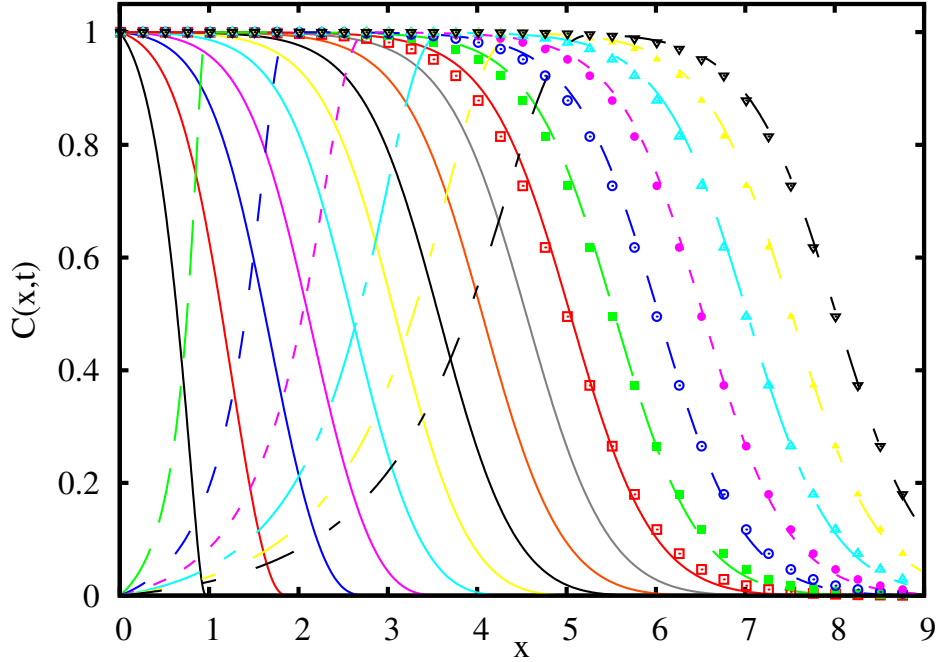
Figure 3.7: (Color online) As in Fig. 3.6 but for filtering model (3.33), Eq. (3.32) with continuous inverse-square-root trap distribution [Eq. (3.28)]. Parameters are $A = v = C_0 = \rho_{1/2} = 1$, $T = 10$. Symbols show the front solution [Eq. (3.52)] for $t \geq 10$ with front velocity (3.54). The raising parts of the curves are almost identical with those in Fig. 3.6, while there are some quantitative differences in the tails, consistent with the exponential vs power-law long-time asymptotics of the corresponding solutions.

Note that the profiles in Figs. 3.6 and 3.7 are very similar even though the corresponding trap distributions differ dramatically. This illustrates that parameter fitting from a limited set of breakthrough curves is a problem ill-defined mathematically. The complexity and ambiguity of the problem grow with increasing number of traps. In Sec. 3.5 we suggest an alternative computationally simple procedure for parameter fitting using the data from several breakthrough curves differing by the input concentrations.

3.5 Experimental implications

The suggested class of mean-field models is characterized by a large number of parameters. In the discrete case, these are the trap rate constants A_i, B_i and the corresponding

concentrations N_i along with the flow velocity v. In the continuous case, the filtering medium is characterized by the response function $\Sigma(p)$ [see Eq. (3.22)]. In our experience, two or three sets of traps are usually sufficient to produce an excellent fit for a typical experimental break-through curve (not shown). This is not surprising, given the number of adjustable parameters. On the other hand, from Eq. (3.54) it is also clear that the obtained parameters would likely prove inadequate if we change the inlet concentration. The long-time asymptotic form of the effluent during the washout stage would also likely be off.

One alternative to a direct non-linear fitting is to use our result given in Eq. (3.54) [or Eq. (3.36)] for the filtering front velocity as a function of the inlet concentration, C_0. With a relatively mild assumption that all trapping rates coincide, $A_i = A$, one obtains the entire shape of the filtering front [Eq. (3.52)]. Thus, fitting the front profiles at different inlet concentrations C_0 to determine the parameter A and the front velocity $v(C_0)$ can be used to directly measure the response function $\Sigma(p)$.

The suggested experimental procedure can be summarized as follows. (**i**) One should use as long filtering columns as practically possible in order to achieve the front formation for a wider range of inlet concentrations. (**ii**) A set of breakthrough curves $C(L, t)$ for several concentrations C_0 at the inlet should be taken. (**iii**) For each curve, the front formation and the applicability of the simplified model with all $A_i = A$ should be verified by fitting with the front profile [Eq. (3.52)]. Given the column length, each fit would result in the front velocity $v(C_0)$, as well as the inverse front width $p = AC_0$. (**iv**) The resulting data points should be used to recover the functional form of $\Sigma(p)$ and the solution for the full model.

It is important to emphasize that the applicability of the model can be controlled at essentially every step. First, the time-dependence of each curve should fit well with Eq. (3.52). Second, the values of the trapping rate A obtained from different curves should be close. Third, the computed washout curves should be compared with the experimentally obtained break-

through curves. The obtained parameters, especially the details of $\Sigma(p)$ for small p, can be further verified by repeating the experiments on a shorter filtering column with the same medium.

3.6 Conclusions

In this paper, we presented a mean-field model to investigate the transport of colloids in porous media. The model corresponds to the filtration under unfavorable conditions, where trapped particles tend to reduce the filtering capacity, and can also be released back to the flow. The situation should be contrasted with favorable filtering conditions characterized by filter ripening. These two different regimes can be achieved, e.g., by changing pH of the media if the colloids are charged. The unfavorable filtering conditions are typical for filtering encountered in natural environment, e.g., ground water with biologically active colloids such as viruses or bacteria.

The advantages of the model are twofold. It not only fixes some technical problems inherent in the mean-field models based on the CDE but also admits analytical solutions with many groups of traps or even with a continuous distribution of detachment rates. It is the existence of such analytical solutions that allowed us to formulate a well-defined procedure for fitting the coefficients. Ultimately, this improves predictive capability and accuracy of the model.

The need for the attachment and detachment rate distributions under unfavorable filtering conditions has already been recognized in the field[51, 52, 53]. Previously it has been implemented in computer-based models in terms of *ad hoc* distributions of the pore radii[54, 56, 57]. Such models could result in good fits to the experimental breakthrough curves. However, we showed in Sec.3.5 that the relevant experimental curves are often insensitive to the details of the trap parameter distributions, especially on the early stages of filtering.

On the other hand, our analysis of the filtering front reveals that the front velocity as

a function of the inlet colloid concentration, $v(C_0)$ [Eq. (3.36)], is *primarily* determined by the distribution of the attachment and detachment rates characterizing the filtering medium. We, indeed, suggest that the filtering front velocity is one of the most important characteristics of the deep-bed filtration as it is directly related to the loss of filtering capacity.

We have developed a detailed protocol to calculate the model parameters based on the experimentally determined front velocity, $v(C_0)$. We emphasize that the most notable feature of the model is its ability to distinguish between permanent traps (straining) and the traps with small but finite detachment rate. It is the latter traps that determine the long-time asymptotics of the washout curves.

The suggested model is applicable to a wide range of problems in which macro-molecules, stable emulsion drops, or pathogenic micro-organisms such as bacteria and viruses are transported in flow through a porous medium. While the model is purely phenomenological in nature, the mapping of the parameters with the experimental data as a function of flow velocity and colloid size will shed light on the nature of trapping for particular colloids. The model can also be extended to account for variations in attachment and detachment rates for various colloids as needed to explain the steep deposition profiles near the inlet of filters[50].

Chapter 4

Conclusions

In conclusion, during my Ph.D. work I have studied the interactions of the microscopic biological particles in equilibrium system, where the focus is on the thermal fluctuation-induced forces between two foreign inclusions in a biological fluid membrane, and in the non-equilibrium system, where the transport and deposition dynamics of the virus like particles (VLPs) in saturated porous media under unfavorable filtering conditions are modeled.

In the first work, we develop an exact method to calculate thermal Casimir forces between inclusions of arbitrary shapes and separation, embedded in a fluid membrane whose fluctuations are governed by the combined action of surface tension, bending modulus, and Gaussian rigidity. Each objects shape and mechanical properties enter only through a characteristic matrix, a static analog of the scattering matrix. We calculate the Casimir interaction between two elastic disks embedded in a membrane. In particular, we find that at short separations the interaction is strong and independent of surface tension.

In the second work, we study the transport and deposition dynamics of colloids in saturated porous media under unfavorable filtering conditions. As an alternative to traditional convection-diffusion or more detailed numerical models, we consider a mean-field description in

which the attachment and detachment processes are characterized by an entire spectrum of rate constants, ranging from shallow traps which mostly account for hydrodynamic dispersivity, all the way to the permanent traps associated with physical straining. The model has an analytical solution which allows analysis of its properties including the long-time asymptotic behavior and the profile of the deposition curves. Furthermore, the model gives rise to a filtering front whose structure, stability, and propagation velocity are examined. Based on these results, we propose an experimental protocol to determine the parameters of the model.

Although biological systems are consist of complex biological entities, with the proper physics modeling and methods, we are able to simplify these complicated systems and unveil the fundamental mechanisms behind them. These studies have greatly deepened our understandings on the biological systems around us and will eventually lead people to uncover the enormous interesting phenomena in the biology world.

Appendix A

A.1 Elastic energy and effective surface tension of inclusion

We assume any point P on the membrane surface originally located at $\vec{r} = (x, y, z)$. When the fluid membrane with a single inclusion fluctuates, the point P moves to the new position P' located at $\vec{v} \equiv (v_x, v_y, v_z)$. Define $\vec{u} \equiv \vec{v} - \vec{r}$ as the vector displacement from P to P'. Inside of the disk (circular inclusion), we denote $\vec{\rho} \equiv \alpha \mathbf{r} \equiv (\xi, \eta, \zeta)$. This is stretched coordinate. Actual disk radius becomes $R \equiv \alpha R_0$ when the strain is applied to the elastic inclusion due to the effect of surface tension of the fluid membrane. The total energy is the sum given by the following terms (up to quadratic order):

The first term describes the energy outside of the inclusions:

$$U_0 \equiv \sigma_0 \left\{ -\pi R^2 + \int_{|\vec{\rho}|>R} d^2\rho \left[(\partial_\xi u_z)^2 + (\partial_\eta u_z)^2 + \partial_\xi u_x \partial_\eta u_y - \partial_\xi u_y \partial_\eta u_x \right] - R \oint_0^{2\pi} d\phi \, u_\rho(R, \phi) + \right\} + U_0^{(B)}$$

where $U_0^{(B)}$ represents the bending energy of the fluid membrane which has the standard form as

$$U_0^{(B)} = \int_{|\vec{\rho}|>R} d^2\rho \left\{ \frac{\kappa_0}{2} \left[\partial_{\xi\xi} u_z + \partial_{\eta\eta} u_z \right]^2 + \bar{\kappa}_0 (\partial_{\xi\xi} u_z \partial_{\eta\eta} u_z - (\partial_{\xi\eta} u_z)^2) \right\} \qquad (A.1)$$

62

The second term gives the line tension energy of the boundary

$$U_\gamma \equiv \gamma \oint_0^{2\pi} d\phi \left| \partial_\phi \vec{\rho}(R, \phi) \right| = \gamma \oint d\phi \left\{ R + u_r + \frac{1}{2R} \left[(\partial_\phi u_r)^2 + (\partial_\phi u_z)^2 \right] \right\}$$

The next two terms are the elastic uniform deformation energy associated the area change of the inclusion

$$
\begin{aligned}
\frac{2U_d}{E} &= \int_{r<R_0} d^2r \left| \partial_x \vec{v} \times \partial_y \vec{v} \right| = \pi R_0^2 (\alpha^2 - 1)^2 + 2\alpha^2(\alpha^2 - 1) \int d^2r (\partial_\xi u_x + \partial_\eta u_y) \\
&+ \alpha^4 \int d^2r (\partial_\xi u_x + \partial_\eta u_y)^2 \\
&+ \alpha^2(\alpha^2 - 1) \int d^2r (\partial_\xi u_z)^2 + (\partial_\eta u_z)^2 + 2\partial_\xi u_x \partial_\eta u_y - 2\partial_\xi u_y \partial_\eta u_x
\end{aligned}
$$

and elastic shear deformation energy associated the shape change of the inclusion:

$$\frac{2U_s}{\Sigma} = \int_{r<R_0} d^2r \frac{|\partial_x \vec{v} \cdot \partial_y \vec{v}|^2}{|\partial_x \vec{v}|^2 |\partial_y \vec{v}|^2} = \int_{r<R_0} d^2r (\partial_x u_y + \partial_y u_x)^2$$

The last term $U_i^{(B)}$ gives the bending energy of the inclusion which has the same form of Eq. (A.1) except the different bending rigidities $\kappa, \bar{\kappa}$ and region $|\vec{\rho}| < R$.

To zeroth order in $\vec{u}$ we have to minimize

$$U^{(0)} = -\pi\sigma_0 R^2 + 2\pi\gamma R + \frac{E}{2}\pi R_0^2 (\alpha^2 - 1)^2,$$

which gives

$$-\sigma_0 + \frac{\gamma}{\alpha R_0} + E(\alpha^2 - 1) = 0, \tag{A.2}$$

and

$$-3\gamma + 2R(E + \sigma_0) > 0 \tag{A.3}$$

63

where Eqs. (A.2) and(A.3) are obtained by using $\partial_\alpha U^{(0)} = 0$ and $\partial_{\alpha,\alpha} U^{(0)} > 0$. Applying Eq. (A.2), we find terms of linear order in $\vec{u}$ disappear as a result:

$$
\begin{aligned}
U^{(1)} &= -\sigma_0 R \oint d\phi\, u_r + \gamma \oint d\phi\, u_r + E\alpha(\alpha^2 - 1) R_0 \oint d\phi\, u_r \\
&= \left[-\sigma_0 + \frac{\gamma}{R_0} + E(\alpha^2 - 1) \right] \alpha R_0 \oint d\phi\, u_r = 0
\end{aligned}
$$

Terms of quadratic order in $\vec{u}$ can be separated into those depending on u_x, u_y and those depending on $u_z \equiv u$:

$$
\begin{aligned}
U_\parallel &= \frac{\Sigma}{2} \int_{r<R_0} d^2 r (\partial_x u_y + \partial_y u_x)^2 + \frac{E}{2} \int_{r<R_0} d^2 r (\partial_\xi u_x + \partial_\eta u_y)^2 + \ldots \\
U_\perp &= \frac{\sigma_0}{2} \int_{\rho>R} d^2\rho (\nabla u)^2 + \frac{\gamma}{2R} \oint d\phi\, (u'_\phi)^2 \Big|_{\rho=R} + E\alpha^2(\alpha^2 - 1) \int_{r<R_0} d^2 r\, (\nabla u)^2 + U_i^{(B)} + U_0^{(B)} \\
&= \frac{\sigma_0}{2} \int_{\rho>R} d^2\rho (\nabla u)^2 + \frac{\gamma}{2R} \oint d\phi\, (u'_\phi)^2 \Big|_{\rho=R} + \frac{E}{2}(\alpha^2 - 1) \int_{\rho<R} d^2\rho (\nabla u)^2 + U_i^{(B)} + U_0^{(B)} \\
&= \frac{\sigma_0}{2} \int_{\rho>R} d^2\rho (\nabla u)^2 + \frac{\gamma}{2R} \oint d\phi\, (u'_\phi)^2 \Big|_{\rho=R} + \frac{1}{2} \underbrace{\left(\sigma_0 - \frac{\gamma}{R} \right)}_{\sigma} \int_{\rho<R} d^2\rho (\nabla u)^2 + U_i^{(B)} + U_0^{(B)}
\end{aligned}
$$

(A.4)

As mentioned in the Sec. 2.2, the fluid membrane does not transmit the in-plane stress perturbations. Thus, only the fluctuations in z direction matters in our case. As a result of Eq. (A.4), we define $\sigma = \sigma_0 - \gamma/R$ as effective inclusion surface tension of the inclusion. Clearly, the σ and σ_0 differ by the amount of additional pressure due to line tension, γ/R. The conclusion can also be applied to a fluid membrane with more than one inclusions.

A.2 Geometry
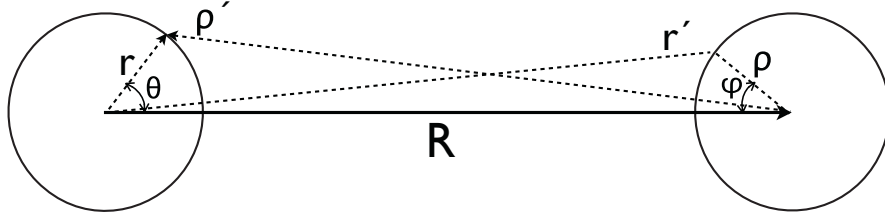

Figure A.1: two-disk geometry and notations: $\mathbf{r} = (r\cos\theta, r\sin\theta)$, $\vec{\rho} = (R - \rho\cos\varphi, \rho\sin\varphi)$

Here, we used $\vec{\rho}' = -\mathbf{R} + \mathbf{r}$, $(\rho')^2 = R^2 + r^2 - 2Rr\cos\theta$, and $\mathbf{r}' = \mathbf{R} + \vec{\rho}$,

$(r')^2 = R^2 + \rho^2 - 2\rho R\cos\varphi$. To convert between the angles, use

$$\cos\varphi' = \frac{R - r\cos\theta}{\rho'} = \frac{R - a\cos\theta}{(R^2 + a^2 - 2Ra\cos\theta)^{1/2}}, \quad \sin\varphi' = \frac{r\sin\theta}{\rho'} = \frac{a\sin\theta}{(R^2 + a^2 - 2Ra\cos\theta)^{1/2}},$$

$$\cos\theta' = \frac{R - \rho\cos\varphi}{r'} = \frac{R - a\cos\varphi}{(R^2 + a^2 - 2Ra\cos\varphi)^{1/2}}, \quad \sin\theta' = \frac{r\sin\varphi}{r'} = \frac{a\sin\varphi}{(R^2 + a^2 - 2Ra\cos\varphi)^{1/2}}.$$

A.3 Derivation of Eq. (2.15)

This appendix provides the mathematical proof that Eq. (2.15) is equivalent to Eq. (2.10). First, substituting Eq. (2.11) into Eq. (2.10), we obtain

$$\beta \Delta \mathcal{F} = -\frac{1}{2} \sum_{n>0} \frac{(-\lambda)^n}{n} \, \mathrm{Tr}[\hat{\mathcal{V}}_{l_1} \hat{G}_0 \hat{\mathcal{V}}_{l_2} \hat{G}_0 \cdots \hat{\mathcal{V}}_{l_{i-1}} \hat{G}_0 \hat{\mathcal{V}}_{l_i} \hat{G}_0 \cdots \hat{\mathcal{V}}_{l_n} \hat{G}_0] \tag{A.5}$$

where $1 \le l_i \le k$. The trace is invariant under the cyclic permutation of $(l_1 l_2 \cdots l_n)$. Thus, if we want to express the result summing over all the terms with the same trace by fixing the first letter of l_1, in general, we should multiply a factor n due to the n possibilities of the cyclic permutations of $(l_1 l_2 \cdots l_n)$. Next, let us group together the subsequent terms with s different indexes in Eq. (A.5),

$$-\frac{1}{2} \frac{(-\lambda)^n}{n} \underbrace{\hat{\mathcal{V}}_{l_1} G_0 \hat{\mathcal{V}}_{l_1} G_0 \cdots \hat{\mathcal{V}}_{l_1} G_0}_{(\hat{\mathcal{V}}_{l_1} G_0)^{n_1}} \underbrace{\hat{\mathcal{V}}_{l_2} G_0 \cdots \hat{\mathcal{V}}_{l_2} G_0}_{(\hat{\mathcal{V}}_{l_2} G_0)^{n_2}} \cdots \underbrace{\hat{\mathcal{V}}_{l_i} G_0 \cdots \hat{\mathcal{V}}_{l_i} G_0}_{(\hat{\mathcal{V}}_{l_i} G_0)^{n_i}} \cdots \underbrace{\hat{\mathcal{V}}_{l_s} G_0 \cdots \hat{\mathcal{V}}_{l_s} G_0}_{(\hat{\mathcal{V}}_{l_s} G_0)^{n_s}} \tag{A.6}$$

where $l_i \ne l_{i+1}$, $l_s \ne l_1$ and $1 \le n_i \le \infty$, $\sum_i n_i = n$. For the fixed s larger than 1, the total sum over all possible n_i in Eq. (A.6) can be written as

$$-\frac{1}{2} \frac{(-\lambda)^s}{s} \underbrace{\hat{\mathcal{V}}_{l_1} (G_0 - \lambda G_0 \hat{\mathcal{V}}_{l_1} G_0 + \cdots)}_{\sum_{n_1 > 0} (-\lambda)^{n_1 - 1} (\hat{\mathcal{V}}_{l_1} G_0)^{n_1}} \underbrace{\hat{\mathcal{V}}_{l_2} (G_0 - \lambda G_0 \hat{\mathcal{V}}_{l_2} G_0 + \cdots)}_{\sum_{n_2 > 0} (-\lambda)^{n_2 - 1} (\hat{\mathcal{V}}_{l_2} G_0)^{n_2}} \cdots \underbrace{\hat{\mathcal{V}}_{l_s} (G_0 - \lambda G_0 \hat{\mathcal{V}}_{l_s} G_0 + \cdots)}_{\sum_{n_s > 0} (-\lambda)^{n_s - 1} (\hat{\mathcal{V}}_{l_s} G_0)^{n_s}} \tag{A.7}$$

which is equivalent to

$$-\frac{1}{2} \frac{(-\lambda)^s}{s} \hat{\mathcal{V}}_{l_1} \hat{G}_\lambda^{(1)} \hat{\mathcal{V}}_{l_2} \hat{G}_\lambda^{(2)} \cdots \hat{\mathcal{V}}_{l_s} \hat{G}_\lambda^{(s)} \tag{A.8}$$

here again if we express the result summing over the terms with the same trace quantity by fixing the first letter l_1, we should multiply a factor m due to the m possibilities of the even permutations of the subsets. By doing so, we can easily see that the factors $1/n$ of Eq. (A.5) and

$1/m$ of Eq. (A.6) both become 1 after multiplying n and m respectively. For $m = 1$, Eq. (A.6) gives

$$-\frac{1}{2}\sum_{n>0}\frac{(-\lambda\hat{\mathcal{V}}_{l_1}\hat{G}_\lambda^{(l_1)})^n}{n} = \frac{1}{2}\log(1 + \lambda\hat{\mathcal{V}}_{l_1}\hat{G}_\lambda^{(l_1)}) \tag{A.9}$$

which is corresponding to the self-energy terms. Combining Eqs. (A.8) and (A.9), we obtain the Casimir energy

$$\beta\Delta\mathcal{F}_\lambda = \frac{1}{2}\sum_{\{l_1\}}\mathrm{Tr}[\log(1 + \lambda\hat{\mathcal{V}}_{l_1}\hat{G}_\lambda^{(l_1)})] - \sum_{s>1}\frac{(-\lambda)^s}{2s}\sum_{\{l_i\}}\mathrm{Tr}\,\hat{\mathcal{V}}_{l_1}G_\lambda^{(l_1)}\hat{\mathcal{V}}_{l_2}G_\lambda^{(l_2)}\ldots\hat{\mathcal{V}}_{l_s}G_\lambda^{(l_s)},$$

A.4 Boundary conditions

In this Appendix we find that the normal modes of the Hamiltionian given in Eq. (2.2) can be written as

$$
\begin{aligned}
H &= \frac{1}{2}\int dA\ \sigma(\nabla u)^2 + (K+\bar{K})(\nabla^2 u)^2 - \bar{K}\partial_i\partial_j u\partial_i\partial_j u + \oint_{\mathcal{S}} dl\ \frac{\gamma}{2r^2}(u_\theta')^2 \\
&= \frac{1}{2}\int dA\ \sigma(\nabla u)^2 + K(\nabla^2 u)^2 + 2\bar{K}(u_{xx}u_{yy} - u_{xy}u_{xy}) + \oint_{\mathcal{S}} dl\ \frac{\gamma}{2r^2}(u_\theta')^2
\end{aligned}
$$

(A.10)

We Minimize Eq. (A.10) by using variation method and find

$$
\begin{aligned}
\delta H &= \int dA \Bigg\{ \nabla\cdot(\delta u\sigma\nabla u) - \delta u\nabla\cdot(\sigma\nabla u) \\
&+ \nabla\cdot(\kappa\nabla^2 u\nabla\delta u) - \nabla\cdot(\delta u\nabla(\kappa\nabla^2 u) + \delta u\nabla\cdot(\nabla\kappa\nabla^2 u)) \\
&+ (\partial_y(\delta u_y\bar{\kappa}u_{xx}) - \partial_y(\delta u\partial_y(\bar{\kappa}u_{xx})) + \delta u\partial_{yy}(\bar{\kappa}u_{xx})) \\
&+ (\partial_x(\delta u_x\bar{\kappa}u_{yy}) - \partial_x(\delta u\partial_x(\bar{\kappa}u_{yy})) + \delta u\partial_{xx}(\bar{\kappa}u_{yy})) \\
&- (\partial_y(\delta u_x\bar{\kappa}u_{xy}) - \partial_x(\delta u\partial_y(\bar{\kappa}u_{xy})) + \delta u\partial_{xy}(\bar{\kappa}u_{xy})) \\
&- (\partial_x(\delta u_y\bar{\kappa}u_{xy}) - \partial_y(\delta u\partial_x(\bar{\kappa}u_{xy})) + \delta u\partial_{xy}(\bar{\kappa}u_{xy})) \Bigg\} \\
&+ \oint dl\frac{\gamma}{r^2}\Big\{ \partial_\theta(\delta u\partial_\theta u) - (\delta u\partial_{\theta\theta}u) \Big\}
\end{aligned}
$$

(A.11)

or in polar coordinates we have

$$
\begin{aligned}
\delta\mathcal{H} \;=\; & 2\int dA\Bigg\{ \delta u[-\nabla\cdot(\sigma\nabla u)+\nabla^2(\kappa\nabla^2 u)] \\
& + \frac{1}{r}\partial_r[\delta u(r\sigma u_r - r\kappa\partial_r\,\nabla^2 u)+\bar{\kappa}\partial_{r\theta\theta}(\frac{u}{r})+\gamma\partial_{\theta\theta}u] \\
& + \frac{1}{r}\partial_r[\delta u_r(\kappa r\nabla^2 u+\bar{\kappa}(\frac{u_{\theta\theta}}{r}+u_r))]+\ldots \Bigg\},
\end{aligned}
$$

(A.12)

where the subscripts indicate partial derivatives. We only keep the radial derivatives associated with boundary terms because of the cylindrical symmetry of the embedded inclusions. In Eq. (A.12) the linear differential operator $\hat{L}$ can be written as,

$$
\hat{L} = \kappa\nabla^4 - \sigma\nabla^2
$$

(A.13)

if $\kappa(\mathbf{r})$ and $\sigma(\mathbf{r})$ are uniform in the region. The eigenstates of the normal modes $u_n(\mathbf{r})$ asscoiated with the linear differential operator $\hat{L}$ can be obtained from the following equation,

$$
\hat{L}u_n = E_n u_n
$$

(A.14)

by satisfying the essential and natural boundary conditions which can be found in Eq. (A.12),

1. u_n continous

2. $\partial_r u_n$ continous

3. $r\sigma\partial_r u_n - r\kappa\partial_r(\nabla^2 u_n)+\bar{\kappa}\partial_{r\theta\theta}(\frac{u_n}{r})-\frac{\gamma}{r}\partial_{\theta\theta}u_n$ continous

4. $r\kappa\nabla^2 u_n + \bar{\kappa}(\frac{1}{r}\partial_{\theta\theta}u_n + \partial_r u_n)$ continous.

(A.15)

69

A.5 Simplification of the surface integral

Assume that u and v obeys the correct boundary conditions and that $\sigma \nabla^2 u - \kappa \nabla^4 u = 0$ inside of the disk and $\sigma_0 \nabla^2 v - \kappa_0 \nabla^4 v = 0$ outside the disk respectively. Consider

$$
\begin{aligned}
\lambda v \hat{\mathcal{V}} u &\equiv \lambda \int_{\mathcal{A}} d^2 \mathbf{r} \{ \sigma_1 \nabla v \cdot \nabla u + \kappa_1 \nabla^2 v \nabla^2 u + \bar{\kappa}_1 (v_{xx} u_{yy} + v_{yy} u_{xx} - 2 v_{xy} u_{xy}) + \oint dl \frac{\gamma}{r^2} \partial_\theta u \partial_\theta v \} \\
&= \int d^2 \mathbf{r} \Big\{ \sigma [\nabla \cdot (v \nabla u) - v \nabla^2 u] + \kappa [\nabla \cdot (\nabla v \, \nabla^2 u) - \nabla \cdot (v \nabla \nabla^2 u) + v \nabla^4 u] \\
&\quad - \sigma_0 [\nabla \cdot (u \nabla v) - u \nabla^2 v] - \kappa_0 [\nabla \cdot (\nabla u \, \nabla^2 v) - \nabla \cdot (u \nabla \nabla^2 v) + u \nabla^4 v] \\
&\quad + (\bar{\kappa} - \bar{\kappa}_0) [(v_x u_{yy})_x - (v_x u_{xy})_y + (v_y u_{xx})_y - (v_y u_{xy})_x] + \oint dl \frac{\gamma}{r^2} [\partial_\theta (v \partial_\theta u) - v \partial_{\theta\theta} u] \Big\} \\
&= \oint dl \Big\{ \sigma v \partial_n u - \sigma_0 u \partial_n v + \kappa (\partial_n v \, \nabla^2 u - v \partial_n \nabla^2 u) - \kappa_0 (\partial_n u \, \nabla^2 v - u \partial_n \nabla^2 v) \\
&\quad + (\bar{\kappa} - \bar{\kappa}_0) [n_x (v_x u_{yy} - v_y u_{xy}) + n_y (v_y u_{xx} - v_x u_{xy})] + \frac{\gamma}{r^2} [\partial_\theta (v \partial_\theta u) - v \partial_{\theta\theta} u] \Big\},
\end{aligned}
$$

$$(A.16)$$

The term with $\kappa - \kappa_0$ can be rewritten in the polar coordinates as follows [add a factor $a(\bar{\kappa} - \bar{\kappa}_0)$]:

$$
\oint dl [n_x (v_x u_{yy} - v_y u_{xy}) + n_y (v_y u_{xx} - v_x u_{xy})] = \oint dl \Big\{ \frac{v_r}{r^2} u_{\theta\theta} + \frac{v_r}{r} u_r - \frac{v}{r^3} u_{\theta\theta} + \frac{v}{r^2} u_{r\theta\theta} \Big\}
$$

Overall, using the boundary conditions on u, we have

$$
\begin{aligned}
\lambda v \hat{\mathcal{V}} u &= \oint dl \Big\{ \sigma v \partial_n u - \sigma_0 u \partial_n v - \frac{\gamma}{r^2} v \partial_{\theta\theta} u + \kappa(\partial_n v \, \nabla^2 u - v \partial_n \nabla^2 u) \\
&\quad - \kappa_0(\partial_n u \, \nabla^2 v - u \partial_n \nabla^2 v) + (\bar\kappa - \bar\kappa_0)\Big[\frac{v_r}{r^2} u_{\theta\theta} + \frac{v_r}{r} u_r - \frac{v}{r^3} u_{\theta\theta} + \frac{v}{r^2} u_{r\theta\theta}\Big] \Big\} \\
&= \oint dl \Big\{ v \overbrace{\Big[\sigma u_r - \kappa(\nabla^2 u)_r - \frac{\bar\kappa}{r^3} u_{\theta\theta} + \frac{\bar\kappa}{r^2} u_{r\theta\theta} - \frac{\gamma}{r^3}\partial_{\theta\theta} u\Big]}^{Q_3} + v_r \overbrace{\Big[\kappa(\nabla^2 u) + \frac{\bar\kappa}{r^2} u_{\theta\theta} + \frac{\bar\kappa}{r} u_r\Big]}^{Q_4} \\
&\quad - \sigma_0 u \partial_n v - \kappa_0(\partial_n u \, \nabla^2 v - u \partial_n \nabla^2 v) - \bar\kappa_0\Big[\frac{v_r}{r^2} u_{\theta\theta} + \frac{v_r}{r} u_r - \frac{v}{r^3} u_{\theta\theta} + \frac{v}{r^2} u_{r\theta\theta}\Big] \Big\} \\
&= \oint dl \Big\{ v \Big[\sigma_0 u_r - \kappa_0(\nabla^2 u)_r - \frac{\bar\kappa_0}{r^3} u_{\theta\theta} + \frac{\bar\kappa_0}{r^2} u_{r\theta\theta}\Big]_0 + v_r \Big[\kappa_0(\nabla^2 u) + \frac{\bar\kappa_0}{r^2} u_{\theta\theta} + \frac{\bar\kappa_0}{r} u_r\Big]_0 \\
&\quad - \sigma_0 u \partial_n v - \kappa_0(\partial_n u \, \nabla^2 v - u \partial_n \nabla^2 v) - \bar\kappa_0\Big[\frac{v_r}{r^2} u_{\theta\theta} + \frac{v_r}{r} u_r - \frac{v}{r^3} u_{\theta\theta} + \frac{v}{r^2} u_{r\theta\theta}\Big] \Big\} \\
&= \kappa_0 \oint dl \Big\{ v\big[\alpha_0^2 u - (\nabla^2 u)\big]_r + v_r\big[(\nabla^2 u) - \alpha_0^2 u\big] - (\nabla^2 v)\, u_r + (\nabla^2 v)_r\, u \Big\},
\end{aligned}
$$

$$(A.17)$$

Now, we have u obeys $\sigma_0 \nabla^2 u - \kappa_0 \nabla^4 u = 0$ outside the disk. Recall that the general solution of GF is the combination of radial and modified Bessel functions. Let us write $u = p + q$ and $v = \tilde p + \tilde q$, where $\nabla^2 p = 0$ and $\nabla^2 q = \alpha_0^2 q$. Using $\kappa_0 \alpha_0^2 = \sigma_0$, Eq. (A.17) becomes

$$
\begin{aligned}
\lambda v \hat{\mathcal{V}} u &= \kappa_0 \alpha_0^2 \oint dl \Big\{ v\, p_r - v_r\, p + \tilde q_r\, u - \tilde q\, u_r \Big\} \\
&= \sigma_0 \oint dl \big\{ (\tilde p + \tilde q)p_r - (\tilde p_r + \tilde q_r)p + \tilde q_r(p + q) - \tilde q(p_r + q_r) \big\} \\
&= \sigma_0 \oint dl \{ \tilde p\, p_r - \tilde p_r\, p + \tilde q_r\, q - \tilde q\, q_r \} \\
&= \sigma_0 \oint dl \big\{ W[p, \tilde p] + W[\tilde q, q] \big\}
\end{aligned}
$$

$$(A.18)$$

Notice that the expression is teh sum of Wronskians, $W[v, u] = v'u - u'v$.

71

A.6 Evaluation of the scattering matrix elements

Given $\mathbf{r}$, $\mathbf{r}'$, the GF can be generally written as follows

$$2\pi\sigma_0 G_\lambda^{\text{in}}(\mathbf{r},\mathbf{r}') = \sum_{m\mu,\alpha\beta} c_{m\mu}^{(\alpha\beta)} f_{m\mu}^{(\alpha)}(\mathbf{r}) g_{m\mu}^{(\beta)}(\mathbf{r}'),$$

where

$$f_{m\mu}^{(1)}(\mathbf{r}) = r^m (\cos m\theta, \sin m\theta)_\mu, \; f_{m\mu}^{(2)}(\mathbf{r}) = I_m(\alpha r)(\cos m\theta, \sin m\theta)_\mu,$$

$$g_{m\mu}^{(1)}(\mathbf{r}') = (r')^{-m}(\cos m\theta', \sin m\theta')_\mu, \; g_{m\mu}^{(2)}(\mathbf{r}') = K_m(\alpha_0 r')(\cos m\theta', \sin m\theta')_\mu.$$

From Eq. (A.16), we find that the action of $\hat{\mathcal{V}}$ can be written as follows

$$v\hat{\mathcal{V}}u = a\oint d\theta \sum_i v\overleftarrow{A}_i\overrightarrow{B}_i u,$$

where $\overleftarrow{A}_i$, $\overrightarrow{B}_i$ are the differential operators acting to the function on the left/right. Then, the leading-order Casimir energy becomes

$$
\begin{aligned}
\mathcal{C} &= -\frac{\lambda^2}{2}\operatorname{Tr}\left[\hat{\mathcal{V}}^{(a)}\hat{G}_\lambda^{(a)}(\mathbf{r},\mathbf{r}')\hat{\mathcal{V}}^{(b)}\hat{G}_\lambda^{(b)}(\vec{\rho},\vec{\rho}')\right] \\
&= -\frac{\lambda^2 a^2}{2\sigma_0^2}\oint\frac{d\theta}{2\pi}\oint\frac{d\varphi}{2\pi}\sum_{m\mu,\alpha\beta}\sum_{n\nu,\alpha'\beta'}\sum_{i,j}c_{m\mu}^{\alpha\beta}c_{n\nu}^{\alpha'\beta'}\operatorname{Tr}\left[\overleftarrow{A}_i^{(a)}\overrightarrow{B}_i^{(a)}f_{m\mu}^{(a,\alpha)}(\mathbf{r})g_{m\mu}^{(a,\beta)}(\mathbf{r}')\overleftarrow{A}_j^{(b)}\overrightarrow{B}_j^{(b)}f_{n\nu}^{(b,\alpha')}(\vec{\rho})g_{n\nu}^{(b,\beta')}(\vec{\rho}')\right] \\
&= -\frac{\lambda^2}{2\sigma_0^2}\sum_{m\mu,\alpha}\sum_{n\nu,\alpha'}\underbrace{\sum_{\beta',i}c_{n\nu}^{\alpha'\beta'}a\oint\frac{d\theta}{2\pi}\left[g_{n\nu}^{(b,\beta')}(\vec{\rho}')\overleftarrow{A}_i^{(a)}\overrightarrow{B}_i^{(a)}f_{m\mu}^{(a,\alpha)}(\mathbf{r})\right]}_{(\sigma_0/\lambda)\Lambda_{n\nu,m\mu}^{a,\alpha'\alpha}}\underbrace{\sum_{\beta,j}c_{m\mu}^{\alpha\beta}a\oint\frac{d\varphi}{2\pi}\left[g_{m\mu}^{(a,\beta)}(\mathbf{r}')\overleftarrow{A}_j^{(b)}\overrightarrow{B}_j^{(b)}f_{n\nu}^{(b,\alpha')}(\vec{\rho})\right]}_{(\sigma_0/\lambda)\Lambda_{m\mu,n\nu}^{b,\alpha\alpha'}} \\
&= -\frac{1}{2}\sum_{m\mu,\alpha}\sum_{n\nu,\alpha'}\Lambda_{n\nu,m\mu}^{a,\alpha'\alpha}\Lambda_{m\mu,n\nu}^{b,\alpha\alpha'}.
\end{aligned}
$$

Now, the Casimir energy is expressed in terms of the following simple integrals:

$$\Lambda^{a,\alpha'\alpha}_{n\nu,m\mu} \equiv \frac{\lambda a}{\sigma_0} \sum_{\beta'} c^{\alpha'\beta'}_{n\nu} \sum_i \oint \frac{d\theta}{2\pi} \left[g^{(b,\beta')}_{n\nu}(\vec{\rho}') \overleftarrow{A}^{(a)}_i \overrightarrow{B}^{(a)}_i f^{(a,\alpha)}_{m\mu}(\mathbf{r}) \right], \qquad (A.19)$$

$$\Lambda^{b,\alpha\alpha'}_{m\mu,n\nu} \equiv \frac{\lambda b}{\sigma_0} \sum_{\beta} c^{\alpha\beta}_{m\mu} \sum_j \oint \frac{d\varphi}{2\pi} \left[g^{(a,\beta)}_{m\mu}(\mathbf{r}') \overleftarrow{A}^{(b)}_j \overrightarrow{B}^{(b)}_j f^{(b,\alpha')}_{n\nu}(\vec{\rho}) \right]. \qquad (A.20)$$

Substituting Eq. (A.18) into Eq. (A.19), we obtain

$$\begin{aligned}
\Lambda^{a,\alpha'\alpha}_{n\nu,m\mu} &\equiv \frac{\lambda a}{\sigma_0} \sum_{\beta'} c^{\alpha'\beta'}_{n\nu} \sum_i \oint \frac{d\theta}{2\pi} \left[g^{(b,\beta')}_{n\nu}(\vec{\rho}') \overleftarrow{A}^{(a)}_i \overrightarrow{B}^{(a)}_i f^{(a,\alpha)}_{m\mu}(\mathbf{r}) \right] \\
&= c^{\alpha'1}_{n\nu} \delta_{\alpha,1} \underbrace{a \oint \frac{d\theta}{2\pi} W[f^{(a,1)}_{m\mu}(\mathbf{r}), g^{(b,1)}_{n\nu}(\vec{\rho}'),]}_{C^{(1)}_{nm,\nu}} + \delta_{\alpha,2} c^{\alpha'2}_{n\nu} \underbrace{a \oint \frac{d\theta}{2\pi} W[g^{(b,2)}_{n\nu}(\vec{\rho}'), f^{(a,2)}_{m\mu}(\mathbf{r})]}_{C^{(2)}_{nm,\nu}},
\end{aligned}$$
$$(A.21)$$

where we only get diagonal terms $\mu = \nu$. Note that the components of the GF in Eq. (A.18) are taken outside of the disk; they have the general form

$$\begin{aligned}
G_\lambda(\mathbf{r},\mathbf{r}') &= \frac{1}{2\pi\sigma_0} \sum_{m\mu,\alpha\beta} c^{(\alpha\beta)}_{m\mu} f^{(\alpha)}_{m\mu}(\mathbf{r}) g^{(\beta)}_{m\mu}(\mathbf{r}'), \\
g^{(1)}_{m\mu}(\mathbf{r}') &= \frac{1}{(r')^m} (\cos m\theta', \sin m\theta')_\mu, \quad g^{(2)}_{m\mu}(\mathbf{r}') = K_m(\alpha_0 r')(\cos m\theta', \sin m\theta')_\mu, \\
f^{(1)}_{m\mu}(\mathbf{r}) &= \frac{1}{(r)^m} (\cos m\theta, \sin m\theta)_\mu, \quad f^{(2)}_{m\mu}(\mathbf{r}) = K_m(\alpha_0 r)(\cos m\theta, \sin m\theta)_\mu;
\end{aligned}$$

the remaining components $f^{(3)}_{m\mu}(\mathbf{r}) \propto I_m(\alpha_0 r)$ and $f^{(4)}_{m\mu}(\mathbf{r}) \propto r^m$ will not contribute to the Wronskians.

We will use the series expansions. Fig. A.2 shows the geometry of the membrane system. Here, we used $\vec{\rho}' = -\mathbf{R} + \mathbf{r}$, $(\rho')^2 = R^2 + r^2 - 2Rr\cos\theta$, and $\mathbf{r}' = \mathbf{R} + \vec{\rho}$,

73

$(r')^2 = R^2 + \rho^2 - 2\rho R\cos\varphi$. To convert between the angles, use

$$\cos\varphi' = \frac{R - r\cos\theta}{\rho'} = \frac{R - a\cos\theta}{(R^2 + a^2 - 2Ra\cos\theta)^{1/2}}, \quad \sin\varphi' = \frac{r\sin\theta}{\rho'} = \frac{a\sin\theta}{(R^2 + a^2 - 2Ra\cos\theta)^{1/2}},$$

$$\cos\theta' = \frac{R - \rho\cos\varphi}{r'} = \frac{R - a\cos\varphi}{(R^2 + a^2 - 2Ra\cos\varphi)^{1/2}}, \quad \sin\theta' = \frac{r\sin\varphi}{r'} = \frac{a\sin\varphi}{(R^2 + a^2 - 2Ra\cos\varphi)^{1/2}}.$$
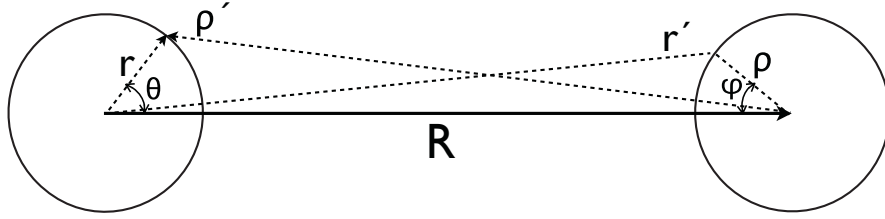

Figure A.2: two-disk geometry and notations: $\mathbf{r} = (r\cos\theta, r\sin\theta)$, $\vec{\rho} = (R - \rho\cos\varphi, \rho\sin\varphi)$

$$
\begin{aligned}
-\ln\rho' &= -\ln(R^2 + r^2 - rR\cos\theta)^{1/2} = -\ln(R) + \sum_{m>0}\frac{r^m\cos m\theta}{mR^m},\\[2mm]
\frac{\cos\varphi'}{\rho'} &= \frac{R - r\cos\theta}{(R^2 + r^2 - rR\cos\theta)} = \sum_{m\geq0}\frac{r^m\cos m\theta}{R^{m+1}}, \quad \frac{\sin\varphi'}{\rho'} = \sum_{m>0}\frac{r^m\sin m\theta}{R^{m+1}},\\[2mm]
\frac{\cos 2\varphi'}{\rho'^2} &= = \sum_{m\geq0}\frac{(m+1)r^m\cos m\theta}{R^{m+2}}, \quad \frac{\sin 2\varphi'}{(\rho')^2} = \sum_{m>0}\frac{(m+1)r^m\sin m\theta}{R^{m+2}},\\[2mm]
\frac{\cos n\varphi'}{\rho'^n} &= = \sum_{m\geq0}\frac{C_m^{m+n-1}r^m\cos m\theta}{R^{m+n}}, \quad \frac{\sin n\varphi'}{\rho'^n} = \sum_{m>0}\frac{C_m^{m+n-1}r^m\sin m\theta}{R^{m+n}}
\end{aligned}
$$

to obtain

$$C_{0m,\nu}^{(1)} = 0, \quad C_{1m,\nu}^{(1)} = -\frac{m}{R^{m+1}}, \quad C_{2m,\nu}^{(1)} = -\frac{m(m+1)}{R^{m+2}}, \quad C_{nm,\nu}^{(1)} = -\frac{mC_m^{m+n-1}}{R^{m+n}}$$

Similarly, the expansions

$$K_0(\alpha_0\rho') = K_0(\alpha_0R)I_0(\alpha_0r) + 2\sum_{m>0}K_m(\alpha_0R)I_m(\alpha_0r)\cos m\theta$$

$$K_1(\alpha_0\rho')\cos\varphi' = K_1(\alpha_0R)I_0(\alpha_0r) + \sum_{m>0}[K_{m-1}(\alpha_0R) + K_{m+1}(\alpha_0R)]I_m(\alpha_0r)\cos(m\theta),$$

$$K_1(\alpha_0\rho')\sin\varphi' = \sum_{m>0}[K_{m+1}(\alpha_0R) - K_{m-1}(\alpha_0R)]I_m(\alpha_0r)\sin(m\theta);$$

$$K_2(\alpha_0\rho')\cos 2\varphi' = K_2(\alpha_0R)I_0(\alpha_0r) + \sum_{m\geq1}[K_{m-2}(R) + K_{m+2}(R)]I_m(\alpha_0r)\cos m\theta$$

$$K_2(\alpha_0\rho')\sin 2\varphi' = \sum_{m\geq1}[K_{m+2}(\alpha_0R) - K_{m-2}(\alpha_0R)]I_m(\alpha_0r)\sin m\theta$$

$$K_n(\alpha_0\rho')\cos n\varphi' = K_n(\alpha_0R)I_0(\alpha_0r) + \sum_{m\geq1}[K_{m-n}(R) + K_{m+n}(R)]I_m(\alpha_0r)\cos m\theta$$

$$K_n(\alpha_0\rho')\sin n\varphi' = \sum_{m\geq1}[K_{m+n}(\alpha_0R) - K_{m-n}(\alpha_0R)]I_m(\alpha_0r)\sin m\theta$$

give [note that $K_{-m}(z) = K_m(z)$]:

$$C_{00,\nu}^{(2)} = \delta_{\nu0}K_0(\alpha_0R), \quad C_{0m,\nu}^{(2)} = \delta_{\nu0}K_m(\alpha_0R), \ m > 0;$$

$$C_{10,\nu}^{(2)} = \delta_{\nu0}K_1(\alpha_0R), \quad C_{1m,\nu}^{(2)} = \frac{K_{m+1}(\alpha_0R) + (-1)^\nu K_{m-1}(\alpha_0R)}{2}, \ m > 0;$$

$$C_{20,\nu}^{(2)} = \delta_{\nu0}K_2(\alpha_0R), \quad C_{2m,\nu}^{(2)} = \frac{K_{m+2}(\alpha_0R) + (-1)^\nu K_{m-2}(\alpha_0R)}{2}, \ m > 0;$$

$$C_{n0,\nu}^{(2)} = \delta_{\nu0}K_n(\alpha_0R), \quad C_{nm,\nu}^{(2)} = \frac{K_{m+n}(\alpha_0R) + (-1)^\nu K_{m-n}(\alpha_0R)}{2}, \ m > 0$$

Now, come back to the infinite-area GF (2.22) immediately outside the disk, $R_> = r'$, $R_< = r$:

$$2\pi\sigma_0 G_\lambda^{(a)}(\mathbf{r},\mathbf{r}') = A_0(r') - \ln(r') + B_0(r')K_0(\alpha_0r) - K_0(\alpha_0r')I_0(\alpha_0r)$$

$$+ \sum_{m>0}\left\{A_m(r')\frac{1}{r^m} + \frac{1}{m}\frac{r^m}{(r')^m} + B_m(r')K_m(\alpha_0r) - 2K_m(\alpha_0r')I_m(\alpha_0r)\right\}\cos m\phi.$$

We can write

$$A_m(r') = \frac{A_m^f}{(r')^m} + A_m^g K_m(\alpha_0 r'), \ m > 0; \quad B_m(r') = \frac{B_m^f}{(r')^m} + B_m^g K_m(\alpha_0 r'), \quad \text{(A.22)}$$

which corresponds to

$$c_{n\nu}^{\alpha'1} = (\delta_{\alpha'1} A_n^f + \delta_{\alpha'2} A_n^g), \quad c_{n\nu}^{\alpha'2} = (\delta_{\alpha'1} B_n^f + \delta_{\alpha'2} B_n^g).$$

Overall, we have [see Eq. (A.21)] for the matrix components in terms of α', α (no summation in ν)

$$\hat{\Lambda}_{n\nu,m\mu} = \delta_{\nu\mu} \begin{pmatrix} A_n^f C_{nm,\nu}^{(1)} & B_n^f C_{nm,\nu}^{(1)} \\ A_n^g C_{nm,\nu}^{(2)} & B_n^g C_{nm,\nu}^{(2)} \end{pmatrix}$$

$$\hat{\Lambda}_{0,0} = K_0 \begin{pmatrix} 0 & 0 \\ A_0^g & B_0^g \end{pmatrix}, \quad \hat{\Lambda}_{0m,\nu} = K_m \begin{pmatrix} 0 & 0 \\ A_0^g & B_0^g \end{pmatrix},$$

$$\hat{\Lambda}_{1,0} = K_1 \begin{pmatrix} 0 & 0 \\ A_1^g & B_1^g \end{pmatrix}, \quad \hat{\Lambda}_{1m,\nu} = \begin{pmatrix} -A_1^f m R^{-m-1} & -B_1^f m R^{-m-1} \\ \frac{A_1^g(K_{m+1}+(-1)^\nu K_{m-1})}{2} & \frac{B_1^g(K_{m+1}+(-1)^\nu K_{m-1})}{2} \end{pmatrix},$$

$$\hat{\Lambda}_{2,0} = K_2 \begin{pmatrix} 0 & 0 \\ A_2^g & B_2^g \end{pmatrix}, \quad \hat{\Lambda}_{2m,\nu} = \begin{pmatrix} -m(m+1)A_2^f/R^{m+2} & -m(m+1)B_2^f/R^{m+2} \\ \frac{A_2^g(K_{m+2}+(-1)^\nu K_{m-2})}{2} & \frac{B_2^g(K_{m+2}+(-1)^\nu K_{m-2})}{2} \end{pmatrix},$$

$$\hat{\Lambda}_{n,m} = K_2 \begin{pmatrix} 0 & 0 \\ A_n^g & B_n^g \end{pmatrix}, \quad \hat{\Lambda}_{nm,\nu} = \begin{pmatrix} -mC_m^{n+m-1}A_n^f/R^{m+n} & -mC_m^{n+m-1}B_n^f/R^{m+n} \\ \frac{A_n^g(K_{m+n}+(-1)^\nu K_{m-n})}{2} & \frac{B_n^g(K_{m+n}+(-1)^\nu K_{m-n})}{2} \end{pmatrix}.$$

Here $K_m \equiv K_m(\alpha_0 R)$.

A.7 The full expressions of A_f, A_g, B_f, B_g

$A_f=$
$$\Big((m-1)\,a^{2\,m}\,\Big(\alpha\,a^2\,\alpha0\,\kappa0\,I_{m+1}(a\,\alpha)\,K_m(a\,\alpha0)\,\big(a^2\,(\alpha^2\,\kappa-\alpha0^2\,\kappa0)+2\,m\,(\kappa0-\kappa)\big)+$$
$$K_{m+1}(a\,\alpha0)\,\big(a\,\alpha\,(\kappa-\kappa0)\,I_{m-1}(a\,\alpha)\,\big(\kappa\,(-a^2\,\alpha^2+m^2+m)-$$
$$\kappa0\,(-a^2\,\alpha0^2+m^2+m)\big)-I_m(a\,\alpha)\,\big(\alpha^2\,a^4\,\kappa\,(\alpha0^2\,\kappa0-\alpha^2\,\kappa)+$$
$$2\,a^2\,\alpha0^2\,\kappa0\,m\,(\kappa-\kappa0)+2\,m^3\,(\kappa-\kappa0)^2+2\,m^2\,(\kappa-\kappa0)^2\big)\big)\Big)\Big)\Big/$$
$$\Big(m\,\Big(a\,\alpha\,I_{m-1}(a\,\alpha)\,\big((\kappa0-\kappa)\,K_{m-1}(a\,\alpha0)\,\big(\kappa\,(m-1)\,(-a^2\,\alpha^2+m^2+m)-$$
$$\kappa0\,(m+1)\,((m-1)\,m-a^2\,\alpha0^2)\big)+a\,\alpha0\,\kappa0\,K_m(a\,\alpha0)$$
$$\big(\kappa0\,(m+1)\,(a^2\,\alpha0^2+2\,m)-\kappa\,(a^2\,\alpha^2\,(m-1)+2\,m\,(m+1))\big)\big)+$$
$$I_m(a\,\alpha)\,\big(2\,a\,\alpha0\,\kappa0\,m\,(m+1)\,K_m(a\,\alpha0)\,\big(a^2\,(\alpha^2\,\kappa-\alpha0^2\,\kappa0)+2\,m\,(\kappa-\kappa0)\big)+$$
$$K_{m-1}(a\,\alpha0)\,\big(\kappa^2\,(m-1)\,(2\,m^2\,(m+1)-a^4\,\alpha^4)-$$
$$\kappa\,\kappa0\,(m+1)\,(4\,(m-1)\,m^2-a^2\,\alpha0^2\,(a^2\,\alpha^2+2\,m))+$$
$$2\,\kappa0^2\,m\,(m+1)\,((m-1)\,m-a^2\,\alpha0^2)\big)\big)\Big)\Big)$$

$A_g=\Big(2\,(m-1)\,a^m$
$$\Big(\frac{1}{a}I_m(a\,\alpha)\,\big(\alpha^2\,a^4\,\kappa\,(\alpha0^2\,\kappa0-\alpha^2\,\kappa)+2\,m^3\,(\kappa-\kappa0)^2+2\,m^2\,(\kappa-\kappa0)^2\big)+$$
$$\alpha\,(\kappa-\kappa0)\,I_{m-1}(a\,\alpha)\,\big(\kappa0\,m\,(m+1)-\kappa\,(-a^2\,\alpha^2+m^2+m)\big)\Big)\Big)\Big/$$
$$\Big(\alpha0\,\Big(a\,\alpha\,I_{m-1}(a\,\alpha)\,\big((\kappa0-\kappa)\,K_{m-1}(a\,\alpha0)\,\big(\kappa\,(m-1)\,(-a^2\,\alpha^2+m^2+m)-$$
$$\kappa0\,(m+1)\,((m-1)\,m-a^2\,\alpha0^2)\big)+a\,\alpha0\,\kappa0\,K_m(a\,\alpha0)$$
$$\big(\kappa0\,(m+1)\,(a^2\,\alpha0^2+2\,m)-\kappa\,(a^2\,\alpha^2\,(m-1)+2\,m\,(m+1))\big)\big)+$$
$$I_m(a\,\alpha)\,\big(2\,a\,\alpha0\,\kappa0\,m\,(m+1)\,K_m(a\,\alpha0)\,\big(a^2\,(\alpha^2\,\kappa-\alpha0^2\,\kappa0)+2\,m\,(\kappa-\kappa0)\big)+$$
$$K_{m-1}(a\,\alpha0)\,\big(\kappa^2\,(m-1)\,(2\,m^2\,(m+1)-a^4\,\alpha^4)-$$
$$\kappa\,\kappa0\,(m+1)\,(4\,(m-1)\,m^2-a^2\,\alpha0^2\,(a^2\,\alpha^2+2\,m))+$$
$$2\,\kappa0^2\,m\,(m+1)\,((m-1)\,m-a^2\,\alpha0^2)\big)\big)\Big)\Big)$$

77

$$B_f = \Bigg(2\,(m-1)\,a^m$$

$$\Bigg(\frac{1}{a} I_m(a\,\alpha)\left(\alpha^2\,a^4\,\kappa\left(\alpha0^2\,\kappa0 - \alpha^2\,\kappa\right) + 2\,m^3\,(\kappa - \kappa0)^2 + 2\,m^2\,(\kappa - \kappa0)^2\right) +$$

$$\alpha\,(\kappa - \kappa0)\,I_{m-1}(a\,\alpha)\left(\kappa0\,m\,(m+1) - \kappa\left(-a^2\,\alpha^2 + m^2 + m\right)\right)\Bigg)\Bigg) \Bigg/$$

$$\Bigg(\alpha0\left(a\,\alpha\,I_{m-1}(a\,\alpha)\left((\kappa0 - \kappa)\,K_{m-1}(a\,\alpha0)\left(\kappa\,(m-1)\left(-a^2\,\alpha^2 + m^2 + m\right) - \right.\right.$$

$$\kappa0\,(m+1)\left((m-1)\,m - a^2\,\alpha0^2\right)\Big) + a\,\alpha0\,\kappa0\,K_m(a\,\alpha0)$$

$$\left(\kappa0\,(m+1)\left(a^2\,\alpha0^2 + 2\,m\right) - \kappa\left(a^2\,\alpha^2\,(m-1) + 2\,m\,(m+1)\right)\right)\Big) +$$

$$I_m(a\,\alpha)\left(2\,a\,\alpha0\,\kappa0\,m\,(m+1)\,K_m(a\,\alpha0)\left(a^2\left(\alpha^2\,\kappa - \alpha0^2\,\kappa0\right) + 2\,m\,(\kappa - \kappa0)\right) + \right.$$

$$K_{m-1}(a\,\alpha0)\left(\kappa^2\,(m-1)\left(2\,m^2\,(m+1) - a^4\,\alpha^4\right) - \right.$$

$$\kappa\,\kappa0\,(m+1)\left(4\,(m-1)\,m^2 - a^2\,\alpha0^2\left(a^2\,\alpha^2 + 2\,m\right)\right) +$$

$$2\,\kappa0^2\,m\,(m+1)\left((m-1)\,m - a^2\,\alpha0^2\right)\Big)\Big)\Big)\Big)\Bigg)$$

$$B_g =$$

$$-\Bigg(2\left(a\,\alpha\,I_{m-1}(a\,\alpha)\left((\kappa0 - \kappa)\,I_{m-1}(a\,\alpha0)\left(\kappa\,(m-1)\left(-a^2\,\alpha^2 + m^2 + m\right) - \kappa0\,(m+\right.\right.$$

$$1)\left((m-1)\,m - a^2\,\alpha0^2\right)\Big) - a\,\alpha0\,\kappa0\,I_m(a\,\alpha0)$$

$$\left(\kappa0\,(m+1)\left(a^2\,\alpha0^2 + 2\,m\right) - \kappa\left(a^2\,\alpha^2\,(m-1) + 2\,m\,(m+1)\right)\right)\Big) +$$

$$I_m(a\,\alpha)\left(2\,a\,\alpha0\,\kappa0\,m\,(m+1)\,I_m(a\,\alpha0)\left(a^2\left(\alpha0^2\,\kappa0 - \alpha^2\,\kappa\right) + 2\,m\,(\kappa0 - \kappa)\right) + \right.$$

$$I_{m-1}(a\,\alpha0)\left(\kappa^2\,(m-1)\left(2\,m^2\,(m+1) - a^4\,\alpha^4\right) - \right.$$

$$\kappa\,\kappa0\,(m+1)\left(4\,(m-1)\,m^2 - a^2\,\alpha0^2\left(a^2\,\alpha^2 + 2\,m\right)\right) +$$

$$2\,\kappa0^2\,m\,(m+1)\left((m-1)\,m - a^2\,\alpha0^2\right)\Big)\Big)\Big)\Big)\Bigg) \Bigg/$$

$$\Bigg(a\,\alpha\,I_{m-1}(a\,\alpha)\left((\kappa0 - \kappa)\,K_{m-1}(a\,\alpha0)\left(\kappa\,(m-1)\left(-a^2\,\alpha^2 + m^2 + m\right) - \right.\right.$$

$$\kappa0\,(m+1)\left((m-1)\,m - a^2\,\alpha0^2\right)\Big) + a\,\alpha0\,\kappa0\,K_m(a\,\alpha0)$$

$$\left(\kappa0\,(m+1)\left(a^2\,\alpha0^2 + 2\,m\right) - \kappa\left(a^2\,\alpha^2\,(m-1) + 2\,m\,(m+1)\right)\right)\Big) +$$

$$I_m(a\,\alpha)\left(2\,a\,\alpha0\,\kappa0\,m\,(m+1)\,K_m(a\,\alpha0)\left(a^2\left(\alpha^2\,\kappa - \alpha0^2\,\kappa0\right) + 2\,m\,(\kappa - \kappa0)\right) + \right.$$

$$K_{m-1}(a\,\alpha0)\left(\kappa^2\,(m-1)\left(2\,m^2\,(m+1) - a^4\,\alpha^4\right) - \right.$$

$$\kappa\,\kappa0\,(m+1)\left(4\,(m-1)\,m^2 - a^2\,\alpha0^2\left(a^2\,\alpha^2 + 2\,m\right)\right) +$$

$$2\,\kappa0^2\,m\,(m+1)\left((m-1)\,m - a^2\,\alpha0^2\right)\Big)\Big)\Big)\Bigg)$$

A.8 PFA

The Casimir energy between two parallel surfaces was derived in Ref. [20]. We use Eq. (2.9) from the paper,

$$\frac{\mathcal{F}_{\text{flat}}}{kTA} = \int \frac{d^D\mathbf{p}}{(2\pi)^D} \ln \tilde{G}^d(\mathbf{p}) + \frac{1}{2} \int \frac{d\mathbf{p}}{(2\pi)^D} \ln \left[1 - \left[\frac{\tilde{G}^d(\mathbf{p}, H)}{\tilde{G}^d(\mathbf{p})} \right]^2 \right] \tag{A.23}$$

where A is the D-dimensional area. Here we focus on the case of the two parallel lines with the separation H immersed in 2-dimensional uniform membrane described by the Hamiltonian of Eq. (2.2). The Green's function is given by

$$G^2(x, y) = \int \frac{d^2p}{(2\pi)^2} \frac{\exp i(p_x x + p_y y)}{\kappa p^4 + \sigma p^2} \tag{A.24}$$

Using this expression, we can evaluate the Fourier transform of the GF defined as following

$$\begin{aligned} \tilde{G}^2(\mathbf{p}, H) &= \int G^d(\mathbf{x}, H) \exp(i\mathbf{p} \cdot \mathbf{x}) d^D\mathbf{x} \\ &= \int dy \int \frac{dp'_x dp'_y}{(2\pi)^2} \frac{\exp i(p'_x H + p'_y y)}{\kappa p'^4 + \sigma p'^2} \exp(ipy) \\ &= \frac{1}{2\sigma} \left\{ \frac{\exp(-pH)}{p} - \frac{\exp(-\sqrt{p^2 + \alpha^2}H)}{\sqrt{p^2 + \alpha^2}} \right\} \end{aligned} \tag{A.25}$$

where $\alpha = \sqrt{\sigma/\kappa}$. Then, substituting Eq. (A.25) into Eq. (A.23) to calculate the free energy density at short distance. In Eq. (A.23), the first term is independent on the separation H, thus, we only calculate the integral of the 2nd term of the formula of our interest. In the following we consider the Casimir energy density for two limiting cases:

- $\alpha \to \infty$, surface tension energy dominated,

$$f_S \equiv \frac{\mathcal{F}_s}{k_B T l} = 2 \times \frac{1}{2} \int_0^\infty \frac{dp}{2\pi} \ln \left[1 - \exp(-2pH) \right] = -\frac{\pi}{24H} \tag{A.26}$$

- $\alpha \to 0$, bending energy dominated,

$$f_B \equiv \frac{\mathcal{F}_{\text{B}}}{k_B T l} = 2 \times \frac{1}{2} \int_0^\infty \frac{dp}{2\pi} \ln\left[1 - \exp(-2pH)(Hp+1)^2\right] = -\frac{0.46}{H} \qquad \text{(A.27)}$$
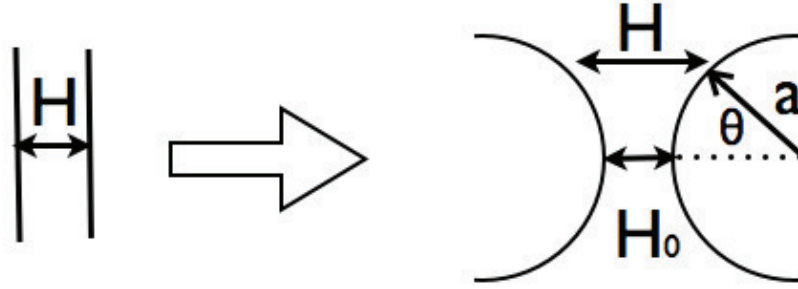
Figure A.3: The interaction between curve edges is expressed as a sum over infinitesimal straight line segments approximated as parallel.

Then integrating over the opposing contact line half circle yields (see Fig. A.3)

$$
\begin{aligned}
\mathcal{F}_{\text{PFA}} &= 2 \int_{H=H_0}^{H=2a+H_0} dy \frac{f}{H} \\
&= 2f \int_0^{\pi/2} d\theta \frac{a \cos\theta}{(2a + H_0) - 2a \cos\theta} \\
&= \frac{2fa}{2a + H_0} \int_0^{\pi/2} \frac{\cos\theta}{1 - \frac{2a}{2a+H_0} \cos\theta} \\
&= \frac{2fa}{2a + H_0} \underbrace{\int_0^{\pi/2} \frac{\cos\theta}{1 - k \cos\theta}}_{I}
\end{aligned}
\tag{A.28}
$$

where $f = -\pi/24$ for surface tension energy dominated and $f = -0.46$(bending only) for

bending energy dominated cases and $k = 2a/(2a + H_0)$. The integration of I is found to be

$$
I = \frac{-\pi \frac{\sqrt{H_0(H_0+4a)}}{(H_0+2a)} + 2\pi}{2\frac{2a}{H_0+2a} \frac{\sqrt{H_0(H_0+4a)}}{H_0+2a}}
\tag{A.29}
$$

Thus we obtain the Casimir energy using PFA

$$
\begin{aligned}
\mathcal{F}_{\text{PFA}} &= \frac{\pi f}{2} \frac{2(H_0 + 2a) - \sqrt{H_0(H_0 + 4a)}}{\sqrt{H_0(H_0 + 4a)}} \\
&= \frac{\pi f}{2} \left(2\sqrt{\frac{a}{H_0}} - 1 + \frac{3}{4}\sqrt{\frac{H_0}{a}} + \cdots\right)
\end{aligned}
\tag{A.30}
$$

81

In the limiting case of surface tension energy dominated, we find

$$\mathcal{F}_{\text{PFA}}^{\text{(S)}} = -\frac{\pi^2}{24}\sqrt{\frac{a}{H_0}} + \frac{\pi^2}{48} - \frac{\pi^2}{64}\sqrt{\frac{H_0}{a}} + \mathcal{O} \tag{A.31}$$

In the limiting case of bending energy dominated, we find

$$\mathcal{F}_{\text{PFA}}^{\text{(B)}} = -1.44\sqrt{\frac{a}{H_0}} + 0.72 - 0.54\sqrt{\frac{H_0}{a}} + \mathcal{O} \tag{A.32}$$

Appendix B

B.1 Velocity of an intermediate front.

Here we derive an inequality for the velocity v_{AB} of an intermediate front interpolating between free-particle concentrations C_A and C_B [Fig. 3.5].

We first write the expressions for the filtering front velocities in clean filter, with the inlet concentrations C_A and $C_B > C_A$ [cf. Eq. (3.35)],

$$\left(\frac{v}{v_A} - 1\right) C_A = \sum_i N_i n_i(C_A),$$

$$\left(\frac{v}{v_B} - 1\right) C_B = \sum_i N_i n_i(C_B).$$

The velocity v_{AB} of the filtering front interpolating between C_A and C_B [Fig. 3.5] is given by

$$\left(\frac{v}{v_{AB}} - 1\right) (C_B - C_A) = \sum_i N_i[n_i(C_B) - n_i(C_A)]. \tag{B.1}$$

Combining these equations, we obtain

$$\frac{C_B}{v_B} - \frac{C_A}{v_A} = \frac{C_B - C_A}{v_{AB}}. \tag{B.2}$$

From here we conclude that the left-hand side (lhs) of Eq. (B.2) is positive. Solving for v_{AB}

and expressing the difference $v_{AB} - v_A$, we have

$$v_{AB} - v_A = \frac{C_B(v_B - v_A)}{\left(\dfrac{C_B}{v_B} - \dfrac{C_A}{v_A}\right) v_B}. \tag{B.3}$$

For the model with saturation [Eq. (3.32)], we saw that $v_B > v_A$, thus $v_{AB} > v_A$.

Bibliography

[1] B. Alberts, A. Johnson, J. Lewis, M. Raff, K. Roberts, and P Walter, Molecular Biology of the Cell (Garland Science, New York, N. Y., 1983).

[2] M. Marsh, ed., Endocytosis, Frontiers in Molecular Biology, (Oxford Univ. Press, Oxford, 2001).

[3] N. Dan, P. Pincus, and S. A. Safran, Membrane-induced interactions between inclusions, Langmuir **9**, 2768 (1993).

[4] M. Goulian, R. Bruinsma, and P. Pincus, Long-Range Forces in Heterogeneous Fluid Membranes, Europhys. Lett. **22**, 145 (1993).

[5] M. Goulian, R. Bruinsma, and P. Pincus, Long-Range Forces in Heterogeneous Fluid Membranes Europhys. Lett. **23**, 155 (1993).

[6] R. Golestanian, M. Goulian, and M. Kardar, Fluctuation-induced interactions between rods on membranes and interfaces Europhys. Lett. **33**, 241 (1996).

[7] R. Golestanian, M. Goulian, and M. Kardar, Fluctuation-induced interactions between rods on a membrane, Phys. Rev. E **54**, 6725 (1996).

[8] Jeong-Man Park, and T. C. Lubensky, Interactions between membrane Inclusions on Fluctuating Membranes, J. Phys. I France **6**, 1217 (1996).

[9] T. R. Weikl, M. M. Kozlov, and W. Helfrich, Interaction of conical membrane inclusions: Effect of lateral tension, Phys. Rev. E **57**, 6988 (1998).

[10] T. Itoh, K. S. Erdmann, A. Roux, B. Habermann, H. Werner, and P. D. Camilli, Dynamin and the Actin Cytoskeleton Cooperatively Regulate Plasma Membrane Invagination by BAR and F-BAR Proteins, Dev. Cell **9**, 791 (2005).

[11] B. J. Reynwar , G. Illya, V. A. Harmandaris, M. M. Müller, K. Kremer, and M. Deserno, Aggregation and vesiculation of membrane proteins by curvature-mediated interactions, Nature **447**, 461 (2007).

[12] K. Farsad, Ringstad N., Takei K., Floyd S., Rose K., De Camilli P., Generation of high curvature membranes mediated by direct endophilin bilayer interactions, J. Cell Biol. **155**, 193 (2001).

[13] T. R. Weikl, Fluctuation-induced aggregation of rigid membrane inclusions, Europhys. Lett. **54**, 547(2001).

[14] W. Rawicz, K. C. Olbrich, T. McIntosh, D. Needham, and E. Evans, Effect of chain length and unsaturation on elasticity of lipid bilayers, Biophys. J. **79**, 328 (2000).

[15] U. Mohideen et al., the unwritten paper (2011).

[16] L. P. Pryadko, and S. Kivelson, and D. W. Hone, Phys. Rev. Lett. **80**, 5651 (1998).

[17] S. J. Rahi, T. Emig, N. Graham, and R. L. Jaffe, and M. Kardar, Scattering theory approach to electrodynamic Casimir forces, Phys. Rev. D **80**, 085021 (2009).

[18] B. V. Derjaguin, I. I. Abrikosova, and E. M. Lifshitz, Direct measurement of molecular attraction between solids separated by a narrow gap, Q. Rev. Chem. Soc. **10**, 295 (1956).

[19] A. R. Evans, M. S. Turner and P. Sens, Interactions between proteins bound to biomembranes, Phys. Rev. E **67**, 041907 (2003).

[20] H. Li, and M. Kardar, Fluctuation-induced forces between rough surfaces, Phys. Rev. Lett. **67**, 3275 (1991).

[21] P. B. Canham, The minimum energy of bending as a possible explanation of the biconcave shape of the human red blood cell, J. Theor. Biol. **26**, 61 (1970).

[22] W. Helfrich, Elastic properties of lipid bilayers: theory and possible experiments, Z. Naturf. C **28**, 693 (1973).

[23] M. Kardar, and R. Golestanian, The "friction" of vacuum, and other fluctuation-induced forces, Rev. Mod. Phys. **71**, 1233 (1999).

[24] H. Hellmann, Einführung in die Quantenchemie, (Franz Deuticke, 1937).

[25] R. P. Feynman, Forces in Molecules, Phys. Rev. **56**, 340 (1939).

[26] E. Noruzifar, and M. Oettel, Anisotropies in thermal Casimir interactions: Ellipsoidal colloids trapped at a fluid interface, Phys. Rev. E **79**, 051401 (2009).

[27] C. Yolcu, I. Z. Rothstein, and M. Deserno, Effective field theory approach to Casimir interactions on soft matter surfaces, arXiv:1007.4760v1(2010).

[28] A. O. Imdakm and M. Sahimi, Transport of large particles in flow through porous media, Phys. Rev. A **36**, 5304 (1987).

[29] L. Bloomfield, Water Filters, Sci. Am. **281**, 152 (1999).

[30] L. Luhrmann, U. Noseck, and C. Tix, Model of contaminant transport in porous media in the presence of colloids applied to actinide migration in column experiments, Water Resour. Res. **34**, 421 (1998).

[31] R. W. Harvey and S. P. Garabedian, Use of colloid filtration theory in modeling movement of bacteria through a contaminated sandy aquifer, **25**, 178 (1991).

[32] J. P. Herzig, D. M. Leclerc, and P. le Goff, Flow of Suspensions through Porous Media—Application to Deep Filtration, Ind. Eng. Chem. **62**, 8 (1970).

[33] C. Tien and A. C. Payatakes, Advances in deep bed filtration, AIChE J. (1979).

[34] H.-W. Chiang and C. Tien, Dynamics of deep-bed filtration. Part I: Analysis of two limiting situations, AIChE J. **31**, 1360 (1985).

[35] S. Vigneswaran and C. J. Song, Mathematical modeling of the entire cycle of deep bed filtration, Water, Air, Soil Pollut. **29**, 155 (1986).

[36] S. Vigneswaran and R. K. Tulachan, Mathematical modelling of transient behaviour of deep bed filtration, Water Res. **22**, 1093 (1988).

[37] C. Ghidaglia. E. Guazzelli and L. Oger, Particle penetration depth distribution in deep bed filtration, J. Phys. D **24**, 2111 (1991).

[38] J. E. Tobiason and B. Vigneswaran, Evaluation of a modified model for deep bed filtration, Water Res. **28**, 335 (1994).

[39] J. Lee and J. Koplik, Simple model for deep bed filtration, Phys. Rev. E **54**, 4011 (1996).

[40] S. Vigneswaran and J. S. Chang, Experimental testing of mathematical models describing the entire cycle of filtration, Water Res. **23**, 1413 (1989).

[41] V. Jegatheesan and S. Vigneswaran, Deep bed filtration: mathematical models and observations, Crit. Rev. Environ. Sci. Technol. **35**, 515 (2005).

[42] O. Albinger, B. K. Biesemeyer, R. G. Arnold, and B. E. Logan, Effect of bacterial heterogeneity on adhesion to uniform collectors by monoclonal populations, FEMS Microbiol. Lett. **124**, 321 (1994).

[43] J. C. Baygents et al., Variation of Surface Charge Density in Monoclonal Bacterial Populations:Implications for Transport through Porous Media, Environ. Sci. Technol. **32**, 1596 (1998).

[44] S. F. Simoni, H. Harms, T. N. P. Bosma, and A. J. B. Zehnder, Population Heterogeneity Affects Transport of Bacteria through Sand Columns at Low Flow Rates, Environ. Sci. Technol. **32**, 2100 (1998).

[45] C. H. Bolster, A. L. Mills, G. M. Hornberger, and J. S. Herman, Spatial distribution of deposited bacteria following Miscible Displacement Experiments in intact cores, Water Resour. Res. **35**, 1797 (1999).

[46] C. H. Bolster, A. L. Mills, G. Hornberger, and J. Herman, Effect of Intra-Population Variability on the Long-Distance Transport of Bacteria, Ground Water **38**, 370 (2000).

[47] J. A. Redman, S. B. Grant, T. M. Olson, and M. K. Estes, Environ. Sci. Technol. **35**, 1798 (2001).

[48] J. A. Redman, M. K. Estes, and S. B. Grant, Resolving macroscale and microscale heterogeneity in virus filtration, Colloids Surf. A **191**, 57 (2001).

[49] N. Tufenkji, J. A. Redman, and M. Elimelech, Interpreting Deposition Patterns of Microbial Particles in Laboratory-Scale Column Experiments, Environ. Sci. Technol., **37**, 616 (2003).

[50] X. Li, T. D. Scheibe, and W. P. Johnson, Apparent Decreases in Colloid Deposition Rate Coefficients with Distance of Transport under Unfavorable Deposition Conditions: A General Phenomenon, Environ. Sci. Technol. **38**, 5616 (2004).

[51] S. A. Bradford, S. Yates, M. Bettahar, and J. Simunek, Physical factors affecting the transport and fate of colloids in saturated porous media, Water Resour. Res. **38**, 1327 (2002).

[52] S. A. Bradford, J. Simunek, M. Bettahar, M. T. van Genuchten, and S. R. Yates, Modeling Colloid Attachment, Straining, and Exclusion in Saturated Porous Media, Environ. Sci. Technol. **37**, 2242 (2003).

[53] J. S. Yoon, J. T. Germaine, and P. J. Culligan, Visualization of particle behavior within a porous medium: Mechanisms for particle filtration and retardation during downward transport, Water Resour. Res. **42**, W06417 (2006).

[54] S. Redner and S. Datta, Clogging Time of a Filter, Phys. Rev. Lett. **84**, 6018 (2000).

[55] W. Hwang and S. Redner, Infiltration through porous media, Phys. Rev. E **63**, 021508 (2001).

[56] Y. S. Kim and A. J. Whittle, Filtration in a Porous Granular Medium: 2. Application of Bubble Model to 1-D Column Experiments, Transp. Porous Media **65**, 309 (2006).

[57] A. Shapiro, P. G. Bedrikovetsky, A. Santos, and O. Medvedev, A stochastic model for filtration of particulate suspensions with incomplete pore plugging, Transp. Porous Media **67**, 135 (2007).

[58] T. D. Scheibe and B. D. Wood, A particle-based model of size or anion exclusion with application to microbial transport in porous media, Water Resour. Res. **39**, 1080 (2003).

[59] L. Lapidus and N. R. Amundson, Mathematics of Adsorption in Beds. VI. The Effect of Longitudinal Diffusion in Ion Exchange and Chromatographic Columns, J. Phys. Chem. **56**, 984 (1952).

[60] T. Jevremovic, *Nuclear Principles in Engineering*, (Springer, New York, 2005), Chap. 7, pp.297-396.

[61] R. Haggerty and S. M. Gorelick, Multiple-rate mass transfer for modeling diffusion and surface reactions in media with pore-scale heterogeneity, Water Resour. Res. **31**, 2383 (1995).

[62] Note that Eq. (3.14) can also be written as a time derivative, $g(x,t) = e^{-\beta x/v - B_1(t-x/v)} \dfrac{\partial}{\partial t} \Big\{ \theta(t - x/v) I_0(\zeta_t) \Big\}$.

[63] C. R. O'Melia and W. Ali, Prog. in Water Technol. **10**, 167 (1978).

[64] H.-W. Chiang and C. Tien, Dynamics of deep-bed filtration. Part I: Analysis of two limiting situations, AIChE J. **31**, 1349 (1984).

[65] D. J. Korteweg and G. de Vries, On the Change of Form of Long Waves Advancing in a Rectangular Canal, and on a New Type of Long Stationary Waves, Philos. Mag. **39**, 422 (1895).

[66] P. G. Drazin, *Solitons*, London Mathematical Society Lecture Note Series, Vol. 85 (Cambridge University Press, Cambridge, 1983).